Multiplex-GAM: genome-wide identification of chromatin contacts yields insights not captured by Hi-C

Robert A. Beagrie[1,2,*], Christoph J. Thieme[1,*], Carlo Annunziatella[3,*], Catherine Baugher[4], Yingnan Zhang[3], Markus Schueler[1,#], Dorothee CA Kramer[1,#], Andrea M. Chiariello[3], Simona Bianco[4], Alexander Kukalev[1], Yichao Li[4], Rieke Kempfer[1], Antonio Scialdone[5], Lonnie R. Welch[4, ‡], Mario Nicodemi[1,3,6‡], Ana Pombo[1,6,7‡]

Addresses:

[1]Epigenetic Regulation and Chromatin Architecture Group, Berlin Institute for Medical Systems Biology, Max-Delbrück Centre for Molecular Medicine, Hannoversche Str. 28, 10115 Berlin, Germany.

[2]Laboratory of Gene Regulation, Weatherall Institute of Molecular Medicine, Oxford, OX39DU, UK.

[3]Dipartimento di Fisica, Università di Napoli Federico II, and INFN Napoli, CNR-SPIN, Complesso Universitario di Monte Sant'Angelo, 80126 Naples, Italy.

[4]School of Electrical Engineering and Computer Science, Ohio University, 45701 Athens, OH, USA.

[5]Institute of Epigenetics and Stem Cells, Helmholtz Zentrum München, Ingolstädter Landstraße 1, 85764 Neuherberg, Germany.

[6]Berlin Institute of Health (BIH), MDC-Berlin, Berlin, Germany.

[7]Humboldt-Universität zu Berlin, 10117 Berlin, Germany.

[*]Joint first authors, [‡]Joint corresponding authors.

Summary (Abstract)

Technologies for measuring 3D genome topology are increasingly important for studying mechanisms of gene regulation, for genome assembly and for mapping of genome rearrangements. Hi-C and other ligation-based methods have become routine but have specific biases. Here, we develop multiplex-GAM, a faster and more affordable version of Genome Architecture Mapping (GAM), a ligation-free technique to map chromatin contacts genome-wide. We perform a detailed comparison of contacts obtained by multiplex-GAM and Hi-C using mouse embryonic stem (mES) cells. We find that both methods detect similar topologically associating domains (TADs). However, when examining the strongest contacts detected by either method, we find that only one third of these are shared. The strongest contacts specifically found in GAM often involve "active" regions, including many transcribed genes and super-enhancers, whereas in Hi-C they more often contain "inactive" regions. Our work shows that active genomic regions are involved in extensive complex contacts that currently go under-estimated in genome-wide ligation-based approaches, and highlights the need for orthogonal advances in genome-wide contact mapping technologies.

Introduction

Our understanding of gene regulation has been dramatically transformed by genome-wide technologies for identifying regulatory elements (e.g. ChIP-seq, ATAC-seq; Andersson and Sandelin, 2020) and by technologies that reveal how these elements are linked to one another through 3D-genome conformation (e.g. Hi-C; Kempfer and Pombo, 2020). However, many cell types of interest are too rare to assay using these methods. Although single-cell variants of Hi-C are available they require purified, disaggregated cell suspensions which can be unachievable for cell types embedded within complex tissues. Furthermore, methods based on chromatin conformation capture (3C) usually focus on contacts between pairs of elements, neglecting higher-order associations. We previously showed that Genome Architecture Mapping (GAM) can identify three-way chromatin contacts and requires only a few hundred cells, with strong enrichment for contacts between regions containing active genes, enhancers and super-enhancers (Beagrie et al., 2017).

The original GAM protocol involves DNA sequencing of many individual thin nuclear slices (which we call nuclear profiles, or NPs), each isolated in random orientations from a different cell in the population. The principle behind GAM is that DNA loci which are physically close to each other in the nuclear space are found in the same NP more frequently than loci which are remote. In the prototype version of GAM, a collection of 200-nm cryosections were cut through a sample of mES cells, before microdissection of single NPs into separate PCR tubes, followed by lengthy manual preparation of sequencing libraries to determine the DNA content of each tube.

First, to reduce the hands-on time required for sequencing hundreds or thousands of NPs, we developed multiplex-GAM. In this variant of GAM, multiple NPs can be added into a single tube and then sequenced together, cutting down on both labour and reagent costs. Second, we optimized the protocol for DNA extraction from NPs such that it is now compatible with liquid dispensing robots, further reducing the time and reagent costs required to generate a GAM dataset. Third, we extended the SLICE statistical model for analysis of GAM data to cover a wider range of experimental parameters (including the addition of multiple NPs per tube). We also use the SLICE statistical model to determine optimal experimental parameters to aid the design of GAM experiments in different cells and organisms. Finally, we produce an extended GAM dataset from mES cells, which we use for comparisons with Hi-C. We show that many contacts are equally detected by both methods, but also identify method-specific contacts, especially those that involve simultaneous associations between three or more genomic elements. We show that GAM is a versatile methodology for mapping chromatin contacts and demonstrate how to design GAM experiments to balance the competing demands of hands-on-time and depth of chromatin contact information.

Results

We previously published a GAM dataset of 408 NPs from mES cells, each isolated from a different nucleus into a single PCR tube (Fig. 1a, original-GAM). We showed that the number of times particular genomic loci are found together in the same NP (their co-segregation) is a measure of their physical proximity in the original population of cells, with high co-segregation values indicating that the regions were close in space. In the first GAM dataset, distant loci are found in the same NP very infrequently (less than 1% of the time; Beagrie et al., 2017). We therefore reasoned that combining more than one NP into a single sequencing library would not reduce our ability to distinguish interacting from non-interacting loci, but could help reduce both reagent costs and the hands-on time required to generate a GAM dataset (Fig. 1a, multiplex-GAM).

To test this intuition, we used a dataset of 480 NPs sequenced individually, which include 408 previously published samples (Beagrie et al., 2017) plus 72 additional NPs (Supplementary Table 1). To simulate multiplex sequencing of two or three NPs, we combined the 480 datasets from single NPs, and generated 240 or 160 *in silico* datasets containing two or three NPs, respectively. We then re-calculated co-segregation matrices from simulated multiplex-GAM datasets and found that these were visually highly similar (Fig. 1b).

To formally understand the effect of including several NPs in multiplex-GAM experimental designs, and to optimize the experimental design parameters, we next updated SLICE, the statistical tool previously developed to reconstruct non-random DNA interaction probabilities in single-cells from locus co-segregation in GAM data (Beagrie et al. 2017). We considered the effects of number of NPs per GAM sample, nuclear ellipticity and NP thickness (Fig. 1c, Supplementary Fig. 1a). To determine the optimal parameters for collection of multiplex GAM datasets in mES cells, we conducted a deeper analysis to determine the dependencies between the minimal number of GAM samples ($m*$) required to detect chromatin contacts with a particular probability of interaction (Pi), given the number of NPs per GAM sample (X_{NP}), cell ellipticity, section thickness (h) and genomic resolution (Fig. 1d). We find that $m*$ increases for smaller resolutions and for weaker interaction strengths (lower Pi), as expected (Fig. 1e,f). We also find that $m*$ remains constant for the range of convenient thicknesses for ultracryomicrotomy, while X_{NP} decreases with increasing cryosection thickness (Fig. 1g).

Finally, we show that the expected co-segregation frequency of two interacting loci is relatively invariant in all but the most extreme ellipsoidal nuclei (Supplementary Fig. 1b).

Based on these novel developments, we made use of the SLICE statistical model to calculate GAM optimal experimental parameters for application to a range of different organisms and cell types. Despite differences in ploidy and nuclear geometry between the selected cell types, we find that the minimum number of tubes (*m**) required to reach a given statistical power is approximately constant (~150 tubes to detect interactions with *Pi* ≥30%) provided that each sample is collected with the optimal number of multiplexed NPs (Supplementary Fig. 1c). Finally, we determined the optimal experimental parameters for producing a new multiplex-GAM dataset in mES cells, and found that *m** reaches a minimum with a multiplexing factor of 3-10 NPs per GAM library (Fig. 1h). A GAM dataset of ~250 libraries each multiplexed with 3 NPs (i.e. obtained from a total of only 750 mES cells) would be sufficient to sample contacts with interaction probabilities above 30% at resolution of 30 kb across all genomic distances, while reducing reagent costs by two thirds (Fig. 1h).

Next, we implemented an improved experimental pipeline for GAM data collection which incorporates staining of the cells for better identification, and shorter or improved steps to facilitate high-throughput experiments, such as storage of laser microdissected NPs, automated pipetting, DNA purification, amplification and sequencing (Fig. 1i). One challenge in the prototype version of GAM was that some cryosections intersect cells without intersecting the nucleus and therefore contain no genomic DNA. In our efforts to identify chemical stains that could allow direct visualisation of nucleus prior to microdissecion, we found that most DNA stains prevent subsequent extraction and/or amplification of DNA from NPs, probably because they bind too strongly or damage DNA (Supplementary Fig. 2a). We therefore collected most of the new multiplex-GAM dataset using a cresyl violet stain which greatly improves identification of cellular profiles during microdissection without affecting DNA extraction (but which does not distinguish the cytoplasm from the nucleus; Fig. 1j, Supplementary Fig. 2b).

In the absence of a direct nuclear stain, we next optimized our multiplex-GAM collection by determining the proportion of cellular slices devoid of NPs. We stained mES cell cryosections for DNA and RNA and found that 23% of profiles intersect the cytoplasm only, with no detectable nuclear material (Supplementary Fig. 2c). As our current GAM pipeline does not distinguish these “cytoplasmic profiles” from NPs, we calculated that adding four cresyl violet stained profiles to each sequencing library would be equivalent to three true nuclear profiles per library on average (Supplementary Fig. 2d).

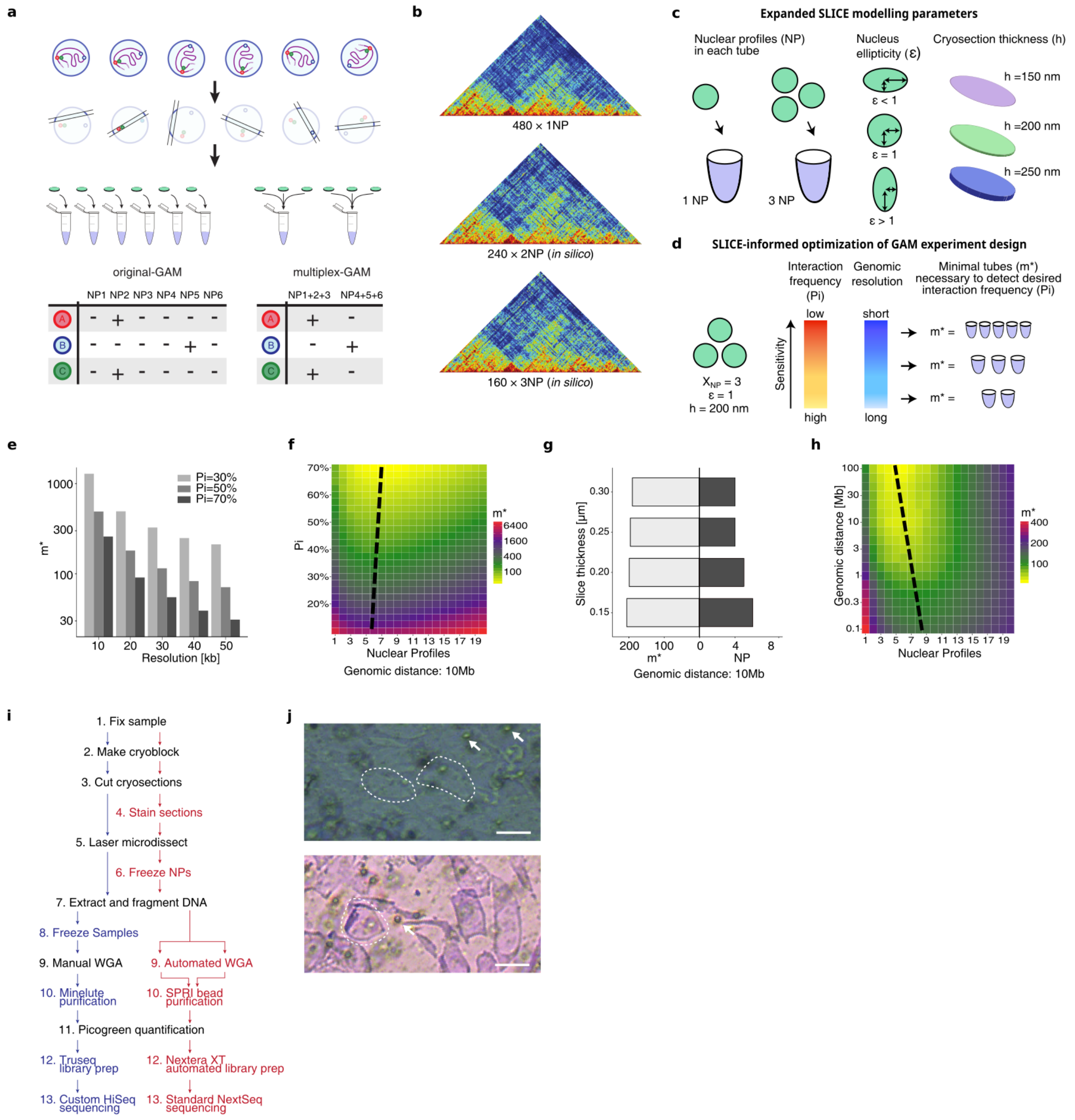

Figure 1

a, In a standard GAM experiment, thin slices from individual nuclei (nuclear profiles or NPs) are isolated by cryosectioning and laser microdissection, then the DNA content of each slice is determined by next generation sequencing. In a multiplex-GAM experiment, DNA from multiple NPs is extracted and sequenced together, reducing sequencing costs. **b**, Multiplex-GAM data constructed *in silico* by combining 1NP datasets. **c**, SLICE accounts for the number of NPs multiplexed in each tube (X_{NP}), the nuclear ellipticity and the thickness of each NP (h) to estimate the minimal number of tubes ($m*$) needed to achieve a given statistical power. **d**, Relationship between the number of tubes required ($m*$), genomic resolution and sensitivity. **e**, $m*$ as a function of genomic resolution and interaction frequency Pi given a genomic distance of 10Mb, X_{NP}=3 and detection efficiencies estimated from the previously published GAM dataset (Beagrie et al., 2017) at the corresponding resolution. **f**, $m*$ as a function of X_{NP} and the interaction probability (Pi) given perfect detection efficiency, a genomic distance of 10Mb and h=220nm, at 30 kb resolution. Grey line marks the approximate position of the minimum value of $m*$ across each row. **g**, Optimal value of X_{NP} and the corresponding value of $m*$ for a range of possible slice thicknesses given Pi =30%, genomic distance of 10Mb and perfect detection. **h**, $m*$ as a function of X_{NP} and the genomic distance given perfect detection, Pi=50% and h=220nm, at 30 kb resolution. Grey line marks the position of the minimum value of $m*$ across each row. **i**, Comparison of the original and multiplex GAM protocols. **j**, Left: unstained nuclear profiles cryosectioned from mES cells. Individual cells are outlined by dashed white lines. White arrows indicate background (bubbles in the microdissection membrane). Right: Cresyl violet stains both cytoplasm and nucleoplasm in mES cell cryosections as visualized by brightfield microscopy, and therefore does not distinguish between cellular profiles that do or do not intersect the nucleus.

To directly test the multiplex-GAM approach with our revised experimental pipeline, we collected a new batch of 245 multiplex GAM sequencing libraries, each containing four cellular sections, from an independent biological replicate from mES cells (Fig. 2a,b). The distribution of quality metrics (most importantly the percentage of mapped reads) was comparable across different collection batches (Supplementary Fig. 3a). The genomic coverage of this dataset (18% of 40 kb windows detected per NP on average) was consistent with the presence of three true NPs per library on average (7% for single NPs, 20% for 3NP *in silico* data; Supplementary Fig. 3b). Comparison of normalized linkage matrices between the 240x3NP multiplex-GAM dataset and the 480x1NP original-GAM dataset indicated that local contact information is well preserved in multiplex-GAM, and conserved between biological replicates (Fig. 2a,b). Erosion analysis of the 3NP-GAM dataset at 40 kb shows that its correlation with the 1NP-GAM dataset resolution begins to saturate at 200x3NPs, indicating that the 245x3NP dataset is large enough to explore chromatin structure at this resolution (Supplementary Fig. 3c).

We next considered the possibility of merging the 1NP and 3NP datasets to increase our power for in-depth comparisons between GAM and Hi-C data. First, we used the 1NP-GAM data to test *in silico* the effect of combining 1NP and 3NP data, and found that matrices from combined 1NP and 3NP libraries retain the quality of 3NP libraries (Supplementary Fig. 4a). Therefore, we merged the experimental 1NP and 3NP datasets to create a combined GAM dataset spanning a total of 1250 NPs each from a different cell (Fig. 2c). To confirm the increased statistical power of the combined 1+3NP dataset, we used SLICE to determine the prominent interactions and compared them with those obtained with the original 408x1NP dataset (Beagrie et al., 2017). Using the deeper 1250 NP dataset from combined 1+3NP GAM data, we detect a greater number of prominent interactions compared to the published data (Fig. 2d,e). These prominent interactions showed a similar pattern of enrichment for genomic features as previously shown in our original 408x1NP mES cell dataset containing only 1NP samples, both for pairwise (Fig. 2f; Supplementary Fig. 4b) and three-way interactions (Fig. 2g).

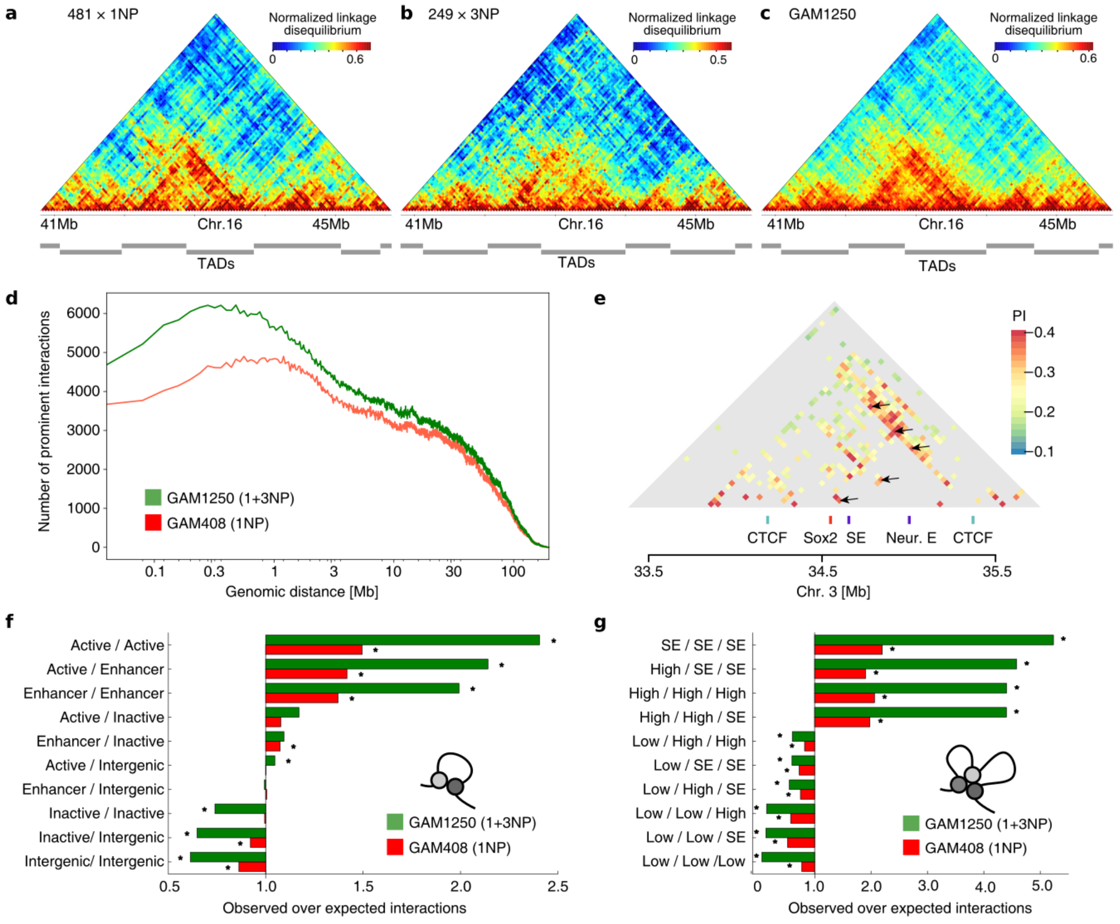

Figure 2

GAM matrices of normalized linkage with a resolution of 40 kb for **a**, multiplex-GAM using 3NPs (249 datasets), **b**, GAM using 1NPs (481 datasets), and **c**, the combined dataset of 1NPs and 3NPs. **d**, Number of prominent interactions identified by SLICE at each genomic distance in the merged GAM-1250 dataset and the published mES GAM dataset (Beagrie et al., 2017). **e**, Contact matrix centered at the Sox2 locus presenting prominent interactions identified by SLICE at 40Kb resolution. Functional elements in the locus are identified below the matrix, and previously identified interactions between these elements are identified by black arrows (Bonev et al., 2017). **f**, Enrichment analysis of pairwise interactions identified by SLICE involving active, inactive, intergenic or enhancer regions for the merged GAM-1250 dataset (green) and the original GAM-408 dataset (red). Statistically significant enrichments/depletions are marked by an asterisk. **g**, Enrichment analysis of triplet interactions identified by SLICE for the merged GAM-1250 dataset (green) and the original GAM-408 dataset (red).

One of the key aims of genome-wide 3D chromatin folding assays is the detection of TADs (Beagan and Phillips-Cremins, 2020). We used the insulation score method (Crane et al., 2015) to identify TAD boundaries in GAM and published Hi-C data (Dixon et al., 2012), choosing parameters that maximized overlap with published TAD boundaries (Methods; Fig. 3a; Supplementary Fig. 5a-d). Of the boundaries identified by GAM, 95% matched a boundary identified by Hi-C, whilst 76% of Hi-C boundaries matched a boundary in GAM (Fig. 3b), comparable to the overlap of boundaries detected from the same Hi-C data using two different computational algorithms (Fig. 3c).

We compared the strength of boundaries detected by only one method with those detected by both GAM and Hi-C. We find that TAD boundaries identified by Hi-C but not GAM

(750 boundaries), or by GAM but not Hi-C (123 boundaries), have weaker insulation than common boundaries (Fig. 3d). To investigate whether the boundaries that are differentially detected between Hi-C and GAM have any distinctive features, we plotted the enrichment of various chromatin marks over TAD boundaries. We confirm the enrichment of previously described features at common boundaries (e.g. common boundaries are enriched for CTCF binding, H3K36me3 and SINE elements, but not for H3K9me3; Fig. 3e; Supplementary Fig. 5e). In most cases, features found at common boundaries are also found at boundaries identified only in GAM or only in Hi-C except with lower enrichment, again suggesting that the strongest boundaries are detected by both methods. The exceptions to this are H3K4me3, RefSeq TSSes, unphosphorylated RNA Polymerase II and CTCF, for which there was a small enrichment at Hi-C only boundaries but not at the smaller number of GAM-only boundaries (Supplementary Fig. 5e). TAD boundaries identified by Hi-C but not by GAM may therefore be a consequence of the fact that GAM detects more contacts between TADs and at longer distances, consistent with the lower Hi-C insulation score of these boundaries and the lack of any specific molecular features distinguishing them from common boundaries.

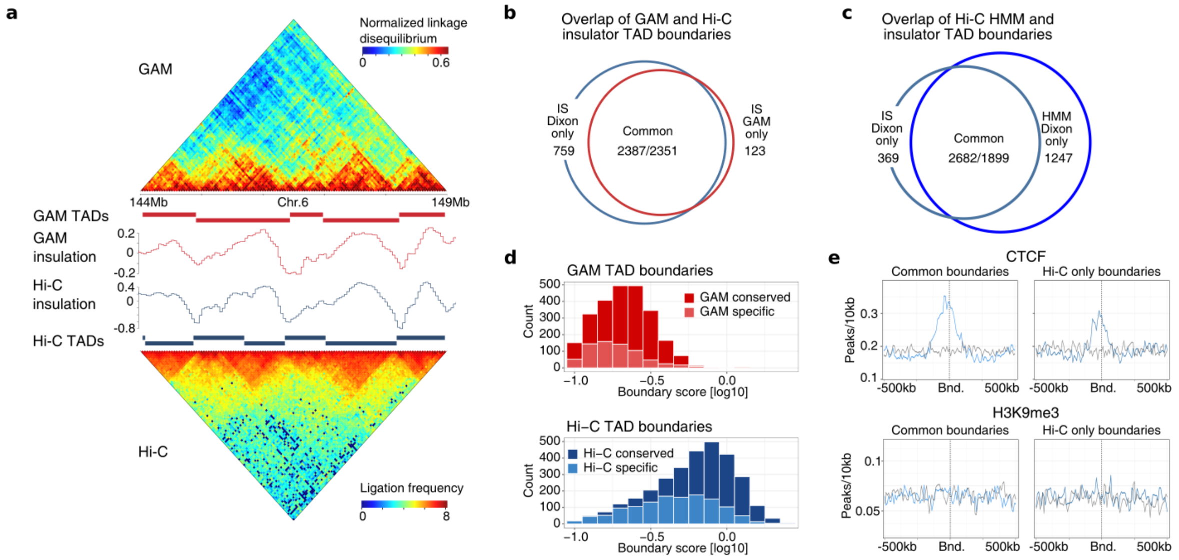

Figure 3
a, Comparison Topological associated domains (TADs) defined by the insulation score method in GAM (top) and Hi-C (Dixon et al., 2012; bottom). **b**, Overlap (within 80 kb distance) of TAD boundaries detected in GAM (red) and Hi-C (blue). **c**, Overlap between insulator score and Hidden Markov Model (HMM) TAD boundary calls from the same Hi-C data. **d**, Boundary strength (drop of insulation score) measured by GAM (red) and Hi-C (blue) for TAD boundaries that are shared between the two methods (dark bars) or only found in a single method (light bars). **e**, Enrichment (blue) of CTCF and H3K9me3 around common or Hi-C-specific TAD boundaries (Bnd.), compared to genomic background (grey).

In visual comparisons between Hi-C and GAM matrices, we also noticed increased contacts across longer genomic distances, spanning several TADs, beyond the levels that we have previously reported for Hi-C (Fraser et al., 2015). We have previously used DNA-FISH to examine two inter-TAD contacts between three regions on chromosome 2 (Fig. 4a). We showed that regions A and B interact more strongly than regions B and C, even though B is approximately equidistant from A and C on the linear genome. We had not previously looked for an interaction between regions A and C, but we noticed that Hi-C measures a weaker contact for the AC than BC regions compared to GAM (Fig. 4a,b). SLICE, which predicts contacts above background for the given genomic distance, reports a much stronger interaction between

AC than BC. Interestingly, single cell measurements by DNA-FISH show a bi-modal distribution of physical distances between regions A and C, suggesting that the two regions indeed interact in a sub-population of cells (44% of measured distances were below 300 nm; Fig. 4c).

To investigate genome-wide differences between GAM and Hi-C in an unbiased fashion, we developed a method for directly comparing matrices derived from the two methods. For these analyses, we considered contacts between loci separated by ≤ 4Mb, as the fidelity of both datasets decreases at larger genomic distances and our simulated multiplex-GAM dataset confirmed that combining NPs in sets of three preserves most of the contact information within this distance (Supplementary Fig. 1d). The selected genomic length scale is useful in most current applications of chromatin contact mapping, in particular, it is sufficient for the detection of enhancer-promoter contacts in most instances.

As GAM detects far more contacts at larger genomic distances, it remained challenging to identify regions with similar or divergent contact patterns between GAM and Hi-C because the numerical output of the two techniques has very different distributions. GAM normalized linkage values range from -1 to +1, whereas Hi-C ligation frequency is dependent on sequencing depth and ranges over many orders of magnitude. We therefore first applied a distance-based z-score normalisation to both datasets (Fig. 4d). Next, we subtracted the two normalized matrices and extracted the most divergent contacts where the difference between the two matrices was greater than the 5% extremes defined by a fitted Normal distribution. We refer to these most divergent contacts as GAM-specific or Hi-C specific contacts (Fig. 4d).

Next, we established a set of strong-and-common contacts that are well detected in both methods by taking the 10% strongest contacts which showed a delta of less than 1 sigma. Many of the strong-and-common contacts are also prominent interactions detected by SLICE analyses of GAM data (Fig. 4e). Strong-and-common contacts and SLICE interactions were more frequently separated by genomic distances below 2Mb (Supplementary Fig. 6a), whereas GAM-specific and Hi-C-specific contacts were slightly depleted at distances <1Mb (Supplementary Fig. 6b). To verify that the GAM-specific and Hi-C specific contacts are indeed strong contacts in each corresponding method (i.e. they are not artefacts of our normalisation procedure) we compared their raw intensities. These analyses confirmed that our approach successfully identifies contacts with high intensity in GAM but low intensity in Hi-C (or vice-versa; Supplementary Fig. 6c). Importantly, whilst many of the strongest contacts in absolute terms were identified by both methods, more than half of the strongest 20% of contacts in GAM or Hi-C were method specific (Fig. 4f).

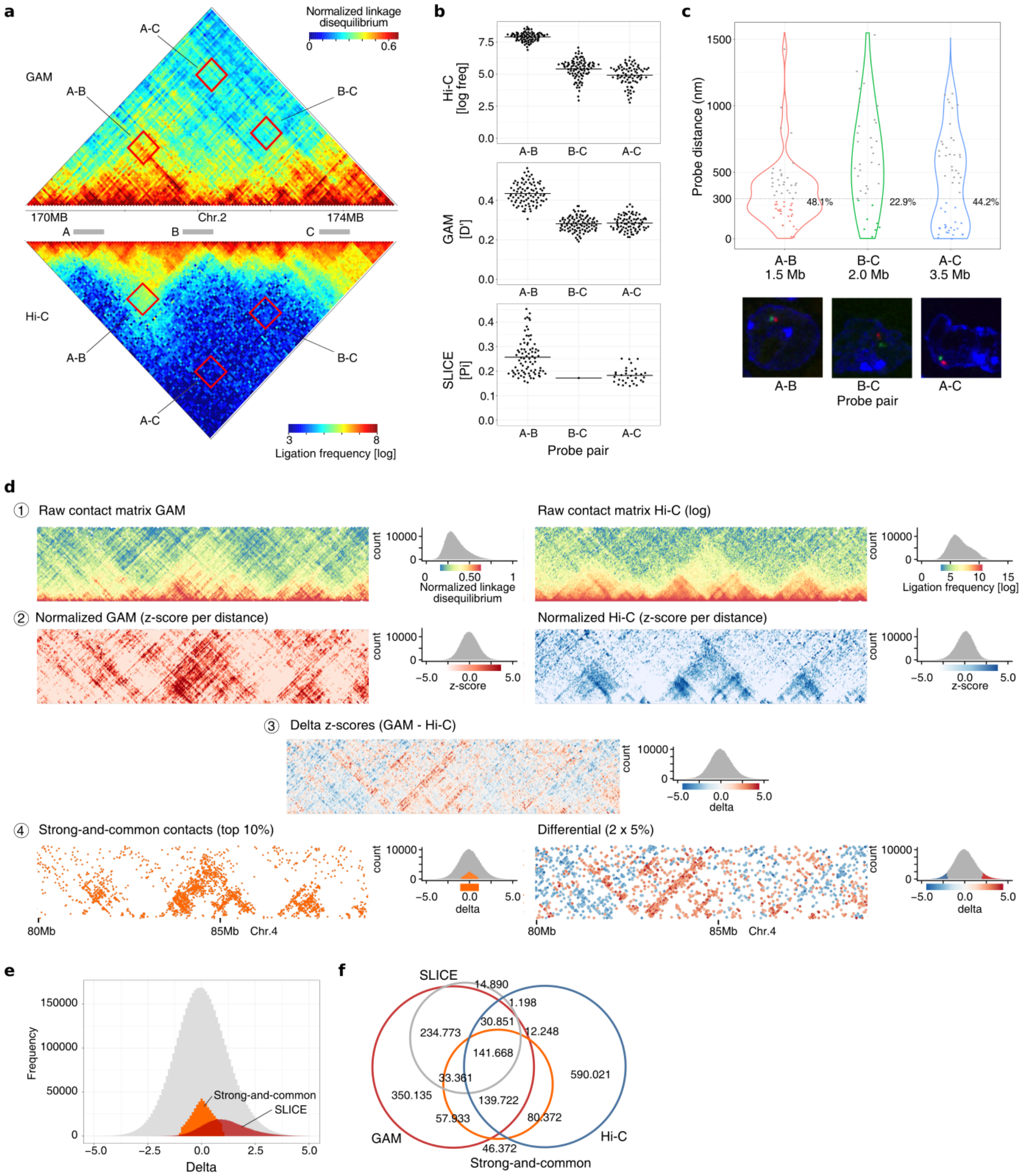

Figure 4

a, Contact matrices showing the locations of loci A, B and C and the contacts between them in GAM (top) and Hi-C (bottom). **b**, Quantification of contacts between the A-B, B-C, and A-C loci by Hi-C (top), GAM (middle) and SLICE (bottom, only interactions with a p-value <0.05 are shown). **c**, Nuclear distances between the A-B, B-C, and A-C loci measured by cryoFISH (top) and representative cryoFISH images (bottom). **d**, Strategy to assess differences and similarities between GAM and Hi-C contact maps. GAM and Hi-C contact data have very different distributions (1), so contacts at the same genomic distance are normalized by z-score transformation (2). Hi-C z-scores are then subtracted from GAM z-scores to generate a delta z-score matrix (3), from which we extract the top 10% of contacts common for both methods (strong-and-common; 4) and the most differential contacts between GAM and Hi-C (GAM-specific or Hi-C specific; 5). **e**, Prominent interactions identified by SLICE shown within the distribution of delta z-scores. **f**, Overlap of the top 20% strongest contacts from GAM and Hi-C with the strong-and-common set and prominent interactions identified by SLICE.

To investigate whether the contacts differentially detected by GAM or Hi-C hold important biological roles, we asked whether they were enriched for particular genomic features. We created a dataset of features including repeat elements, heterochromatin marks, transcription factor binding sites, RNA Polymerase and transcription-related histone marks (Fig. 5a). We then counted the number of contacts in each category (GAM-specific, Hi-C specific, strong-and-common) between each possible pair of features (e.g. CTCF-CTCF, EP300-Nanog, etc.) and looked for feature pairs over-represented (enriched) or under-represented (depleted) from GAM-specific or Hi-C specific contacts relative to distance-matched random backgrounds (Methods; Supplementary Fig. 7a). We found many feature pairs enriched in GAM-specific contacts, whereas only a small number were enriched in Hi-C specific contacts (Supplementary Fig. 7b,c). The feature pairs most enriched in GAM-specific contacts included transcription factors, enhancers and RNA Polymerase II. By contrast, heterochromatin regions (i.e. those marked by H3K9me3 or H3K20me3) were most enriched in Hi-C specific contacts (Fig. 5b). Reassuringly, strong contacts detected by both methods were enriched for CTCF-CTCF contacts, but we find many GAM-specific contacts that connect a CTCF site with an enhancer/CTCF site, whereas these connections were depleted from Hi-C specific contacts (Fig. 5c).

As this analysis is conducted at 40 kb resolution, many contact anchors may contain multiple genomic features (Fig. 5c). We therefore stratified our analysis to account for overlapping feature pair annotations. For example, the GAM-specific, Hi-C specific and strong-and-common contact sets all contain large numbers of CTCF-CTCF contacts. Amongst the GAM-specific contacts, the most common subgroup of CTCF-CTCF contacts were those in which contact anchors also overlapped enhancers and the elongating form of RNAPII (a marker of active genes; 14,403 of 61,212 total CTCF-CTCF contacts). By contrast, in Hi-C-specific and strong-and-common contacts, the most common CTCF-CTCF contacts were those without any other annotation (Hi-C specific: 5930 of 25,236 total CTCF-CTCF contacts, strong-and-common: 20,710 of 89,533). These results suggest that GAM-specific contacts are strongly enriched for a specific subset of CTCF-CTCF contacts that co-occur with enhancer and active genes and which are underestimated in Hi-C data. Indeed, the enhancer-CTCF class of contacts was the most informative in a random-forest model trained to distinguish GAM-specific and Hi-C specific contacts (Fig. 5d).

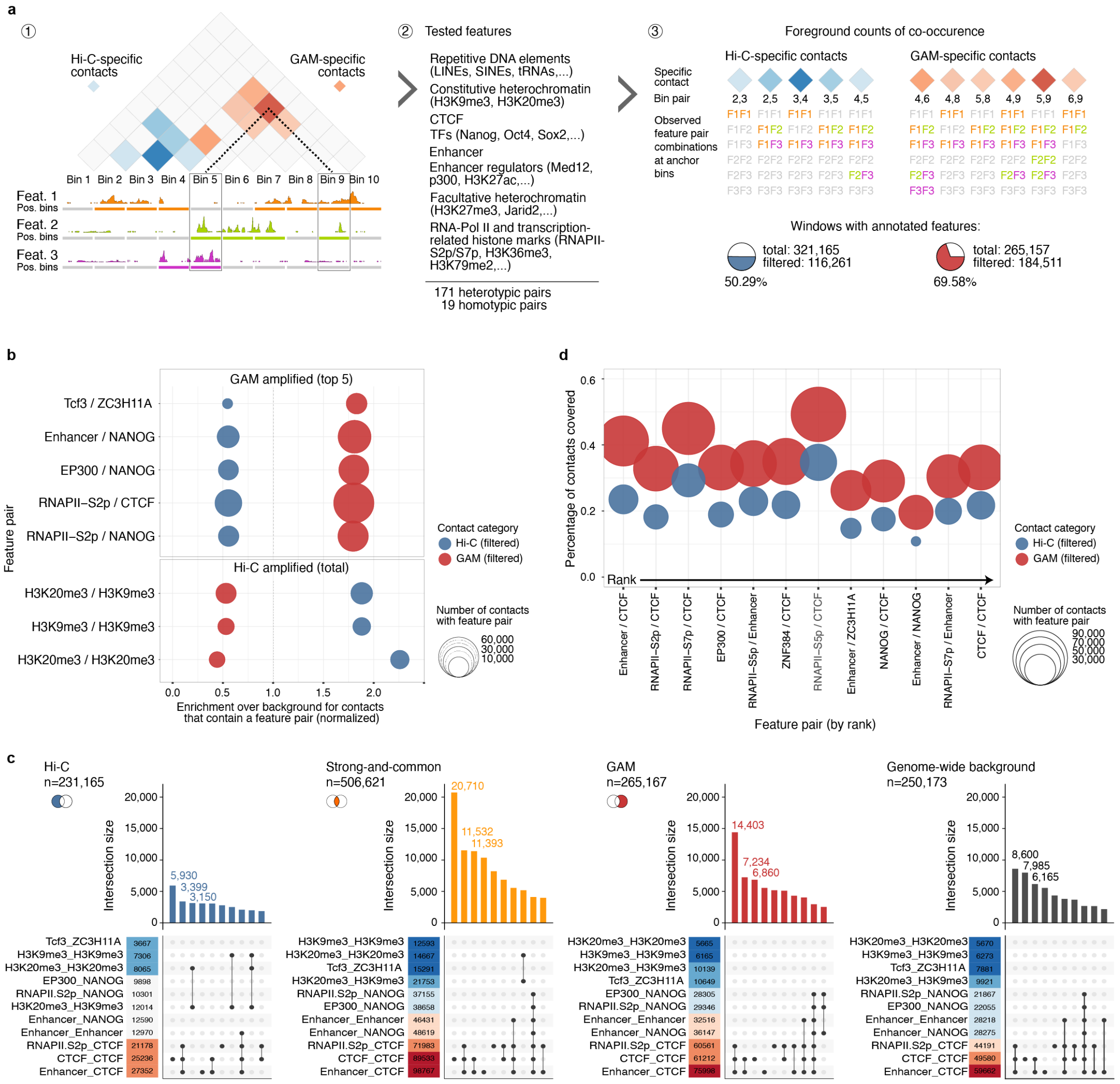

Figure 5

a, Schematic for detecting feature pair enrichments in method-specific contacts (red and blue). (1) Each contact is defined by two genomic anchor points which we categorized as either positive or negative for peaks of the respective feature. (2) We assessed 190 feature pairs and (3) quantified feature occurrences at the anchor points, filtering out contacts with no feature pairs. **b**, Feature pairs with the highest enrichment over background for GAM-specific (top) and Hi-C specific (bottom) contacts. **c**, Upset plots quantifying the co-occurrences of enriched feature pairs in contacts of each subgroup. Occurrence counts for each feature pair are coloured according to their absolute frequency within contacts of each set. **d**, Feature pairs with the highest discriminatory power (by mean decrease of Gini impurity) in random forests trained to separate GAM-specific and Hi-C specific contacts.

Having identified striking enrichments for specific genomic features amongst GAM- and Hi-C-specific contacts, we wondered whether contacts involving genomic regions harbouring specific features might be generally poorly detected by either method. To identify blind-spots in each method, we developed an approach that counted the number of GAM-specific and Hi-C specific contacts formed by each window and looked for regions involved in many more GAM-specific than Hi-C specific contacts or vice versa (Fig. 6a; Supplementary Fig. 8a). Surprisingly, we find that blind-spot windows are not only abundant but also cluster in the linear genome, such that large regions consistently interact more strongly either in GAM or in Hi-C (Fig. 6b). Clusters that form many GAM-specific contacts (GAM-preferred regions) contained more genes and had higher transcriptional activity (Fig. 6c) whilst clusters that form many Hi-C specific contacts (Hi-C preferred regions) were more frequently found in regions associated with the nuclear lamina (Fig. 6d). We further identified that GAM-preferred regions tend to be occupied by CTCF, P300, certain mES cell TFs, RNA Polymerase II (especially the elongating, S2p form), enhancers and super-enhancers, whereas Hi-C preferred regions showed a slight enrichment for the heterochromatin marks H3K20me3 or H3K9me3 (Fig. 6e; Supplementary Fig. 8b).

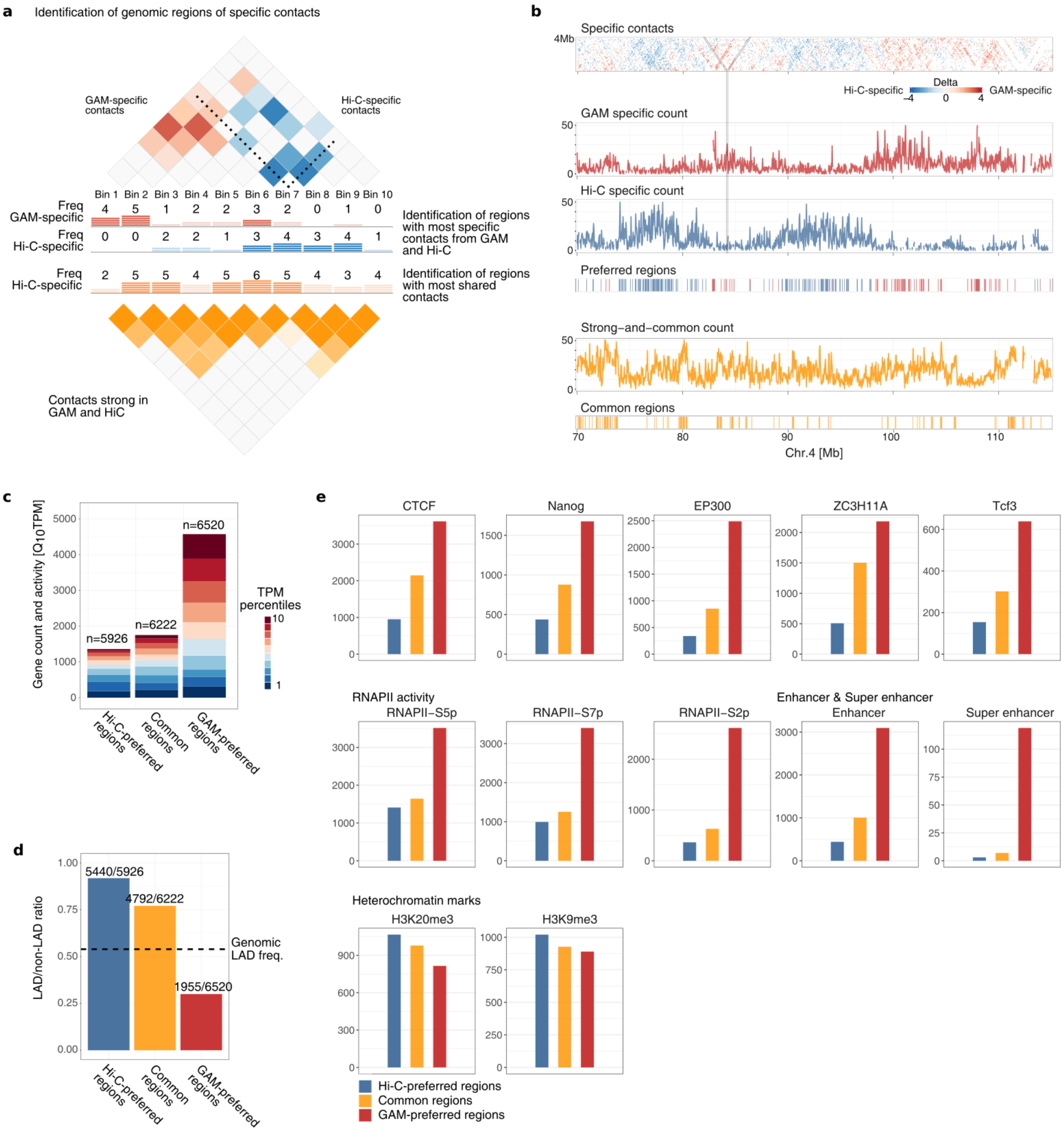

Figure 6

a, Strategy for identifying genomic regions forming many contacts specific to either GAM or Hi-C. We counted how often a genomic region was found to be an anchor point in the set of GAM-specific contacts, Hi-C specific contacts, or strong-and-common contacts. The 10% of genomic bins with the highest absolute difference between the number of GAM-specific and Hi-C specific contacts were classified as Hi-C-preferred regions or GAM-preferred regions, respectively. Similarly, top 10% of strong-and-common contacts were used to define common regions seen equally well by both methods. **b**, Example region on chromosome 4 showing delta z-score matrix (top) and clusters of method-specific preferences designated as Hi-C-preferred regions, GAM-preferred regions or common regions (bottom). **c**, Number of genes and distribution of gene transcriptional activity (TPM) for Hi-C preferred (left), common (middle) and GAM-preferred (right) regions. **d**, Fraction of genomic windows within Lamina Associated Domains (LADs) for Hi-C preferred (left), common (middle) and GAM-preferred (right) regions. Numbers on top of the bar give absolute numbers for LAD windows over the total of windows per category. **e**, Numbers of genomic windows overlapping a range of features.

Since the observed patterns can be partly explained by compartmentalisation, we wondered why GAM and Hi-C might measure different relative contact strengths for these compartments. First, we computed compartment definitions from GAM and Hi-C data. Next, we measured the proportion of GAM- or Hi-C-preferred regions that belong to compartments A or B (the active or inactive compartments, respectively), and found that GAM-preferred regions are highly enriched for chromatin belonging to compartment A, whereas Hi-C-preferred regions and strong-and-common regions are enriched within the B compartment (Fig. 7a; Supplementary Fig. 9).

Finally, we considered whether the enrichment in GAM-preferred regions for active features (active genes, TFs, polymerase, enhancers and compartment A), could be due to different levels of contact complexity, i.e. to interactions with many simultaneous interacting partners. Complex interactions are expected to be underestimated in Hi-C datasets because the ligation step only allows for the measurement of two interacting partners per restriction fragment in each cell where the contact is established (O'Sullivan et al., 2013) (Fig. 7b).

To investigate the relationship between interaction complexity and the differences in method-specific contacts and method-preferred regions, we used SLICE to predict the probability of interaction for all possible sets of three 1Mb windows lying on the same chromosome (i.e. the Pi_{ABC} for all possible triplets of loci A, B and C; Beagrie et al., 2017). We then calculated the mean Pi_{ABC} across all triplets involving a particular window. Mean Pi_{ABC} measures the number of distinct interactions formed by each window that have at least two other partners, and is therefore a measure of interaction complexity. We find that windows in the A compartment indeed form more complex interactions than windows in the B compartment. Interestingly, windows that formed many GAM-specific contacts had a much higher complexity than windows that establish strong-and-common or Hi-C-specific contacts even when comparing within the same compartment (Fig. 7c). All the genomic features associated with GAM-specific contacts were also associated with greater interaction complexity, with the strongest effect seen for the S2p phosphoisoform of RNA Polymerase II and for super-enhancers, in line with our previous work which identified long-range chromatin contacts between super-enhancers and actively-transcribed genomic regions across tens of megabases (Fig. 7d). These results suggest the existence of abundant chromatin contacts where many active regions interact simultaneously, which have been so far unappreciated through the use of ligation-based methods.

Finally, we examined whether high interaction complexity might artificially deflate contact probability as measured by Hi-C, since in complex contacts each DNA fragment picks up a given interacting fragment with lower probability. We correlated pairwise contacts from GAM and Hi-C at 1Mb resolution and find that regions with a high complexity generally have higher pair-wise contact scores when measured by GAM, whereas regions of low complexity generally have higher pair-wise contact scores when measured by Hi-C (Fig. 7e). This is particularly evident when we plot only a subset of interacting pairs that all have very similar GAM contact frequency, demonstrating that complexity explains a large amount of the divergence in contact frequencies measured by Hi-C or GAM.

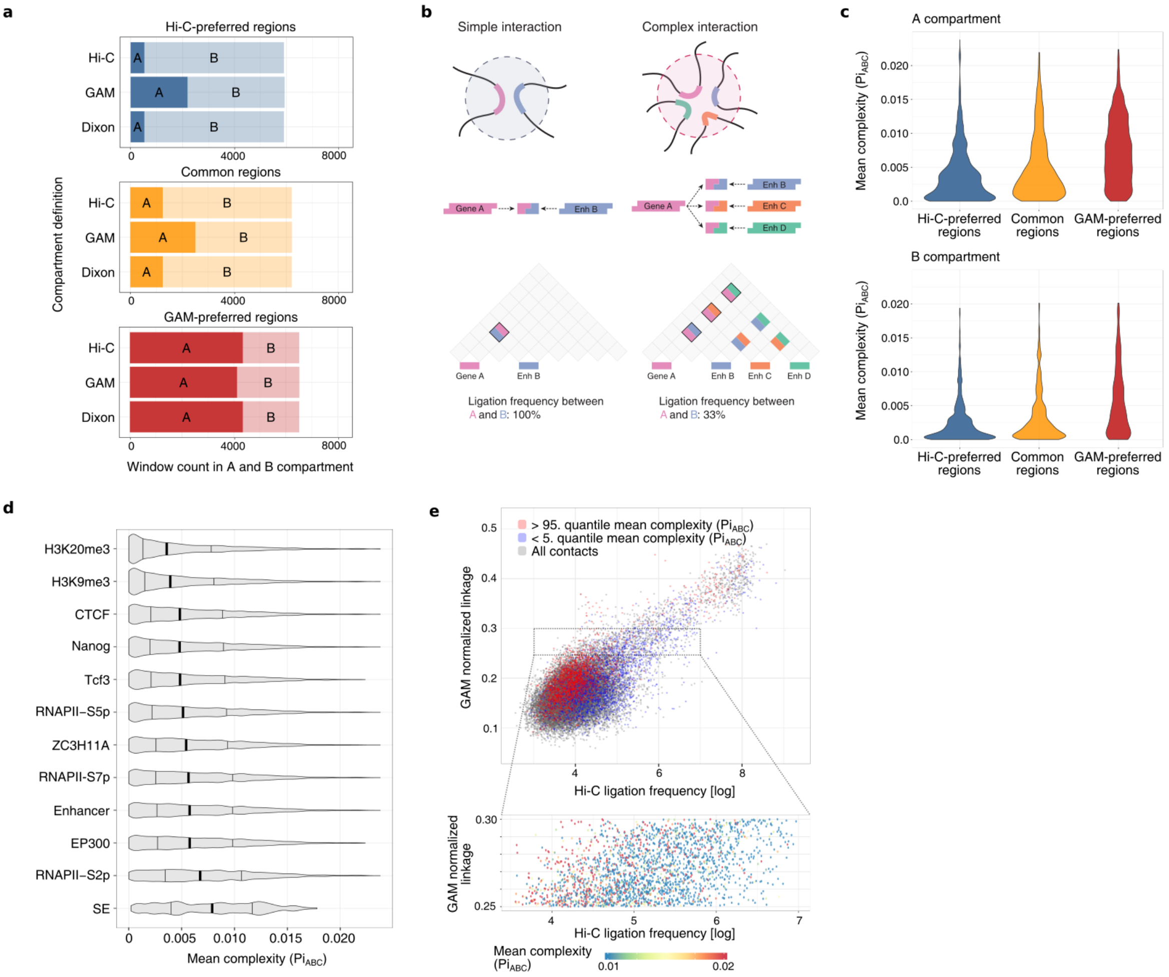

Figure 7

a, Numbers of Hi-C-preferred (left), common (middle) and GAM-preferred (right) regions located A or B compartments calculated by PCA decomposition of Hi-C data (top), GAM data (middle) or published compartments (bottom). **b**, Interaction complexity: simple interactions involve only a few genomic regions, whilst complex interactions involve many genomic regions at once. Ligation events connect two pieces of DNA, so pairwise contacts can be directly determined while measurement of higher order contacts may be affected by competing ligation events. **c**, Contact complexity (measured as the mean Pi_{ABC} – the interaction probability of 1Mb triplets calculated by SLICE) for Hi-C preferred (left), common (middle) or GAM-preferred (right) regions in the A compartment (top) or the B compartment (bottom). **d**, Complexity for genomic bins which are positive for a feature, ranked by increasing mean. **e**, Relationship between pairwise Hi-C ligation frequency (X-axis), pairwise GAM normalized linkage (Y-axis) and complexity (5% pairwise interactions with highest mean Pi_{ABC} in red, lowest 5% in blue). Inset: Hi-C ligation frequency of 1Mb pairwise contacts that have a similar GAM normalized linkage, coloured by complexity.

Discussion

The three-dimensional structure of the nucleus is inextricably linked with its functional roles, including gene regulation, DNA replication and the DNA damage response. Consequently, molecular techniques for measuring the 3D folding of chromatin within the nucleus have been instrumental in advancing our understanding of nuclear function over the past decade (Kempfer and Pombo, 2020). Here, we have developed multiplex-GAM, a new variant of Genome Architecture Mapping that enables faster and more cost-effective analysis of chromatin folding genome-wide than the previous version (Beagrie et al., 2017). GAM requires only a few hundred cells, which is of particular relevance to human genetics where researchers need to assay the 3D contacts made by disease-linked sequence variants in specific, often rare cell types impacted by the disease (e.g. neuronal subtypes in neurodegenerative diseases). We have recently applied Multiplex-GAM to different neuronal subtypes in brain tissues, and discovered abundant cell-type specific contacts that contain differentially expressed genes and accessible regulatory elements (Winick-Ng et al., 2020).

Here, we develop multiplex-GAM and generate a larger GAM dataset, which we use for detailed comparisons between GAM and Hi-C, the most frequently used genome-wide method for chromatin contact analysis (Lieberman-Aiden et al., 2009). We find that GAM and Hi-C detect similar TADs, large folded domains that are thought to constrain gene regulatory elements and form a fundamental unit of chromatin organisation (Dixon et al., 2012; Nora et al., 2012; Sexton et al., 2012). Many strong contacts, including a large proportion of CTCF-mediated loops, are also detected by both methods. By careful examination of finer-scale differences, we identify that chromatin contacts given more weight by GAM frequently connect genomic loci bound by enhancers, key mES cell transcription factors, RNA Polymerase II and CTCF, whereas contacts which feature more prominently in Hi-C matrices connect regions marked by the heterochromatin-associated histone modifications H3K9me3 and H3K20me3.

We then looked for regions of the genome which consistently form more contacts in GAM datasets than in Hi-C datasets and found that these regions are located in large genomic regions bound by the same activating transcription factors identified in the GAM-specific contacts. In our previous work, we found that super-enhancers are the genomic regions most enriched in complex, multi-partner interactions, together with the most actively transcribed regions (Beagrie et al., 2017). We now extend this finding to show that the regions forming strong contacts in GAM also tend to form more complex interactions. Theoretical work has previously suggested that ligation-based methods, such as Hi-C, might underestimate contacts between multiple partners, as ligation only captures two or a few contact partners at a time (O'Sullivan et al., 2013). We find that ligation frequencies measured by Hi-C are systematically lower between regions that form complex interactions, providing the first experimental evidence to support such an effect.

Ligation is not the only potential source of difference between the two methods, as GAM and Hi-C also make use of quite different fixation protocols. The choice of fixation protocol has been shown to affect the proportion of informative ligation events between different 3C experiments (Oudelaar et al., 2017), and it may also influence the contacts of genomic regions with different protein composition and/or compaction within a single experiment (Downes et al., 2020; Williamson et al., 2014). The digestion of nuclear chromatin necessary for preparing Hi-C libraries has also been shown to disrupt nuclear structure (Gavrilov et al., 2013), whereas GAM uses fixation protocols specifically chosen to maximize the preservation of nuclear architecture and retention of nuclear proteins (Guillot et al., 2004). Ultimately, formaldehyde fixation remains a "black box" and will continue to complicate interpretation of the most widely used methods for measuring chromatin structure (including microscopy methods like FISH; Gavrilov et al., 2015). Live-cell imaging methods circumvent the need for fixation and will provide valuable orthogonal data, but these methods currently require recruitment of large numbers of fluorophores which may themselves influence folding (Shaban and Seeber, 2020). Ultimately, it should eventually be possible to shed light on the effect of fixation by extending GAM to unfixed nuclei through sectioning of vitrified samples.

Another factor that may influence method-specific contacts is data processing. It has recently been shown that Hi-C detects fewer contacts between regions of condensed chromatin due to a lower accessibility of these regions to restriction enzyme digestion (Chandradoss et al., 2020). However, matrix-balancing algorithms commonly used to normalize Hi-C data can overcorrect for this effect, leading to an aberrantly high frequency of contacts between condensed domains. Consistent with these results, we find that regions of the genome which consistently form more contacts in normalized Hi-C are enriched for heterochromatin marks. We have found the bias in raw GAM datasets to be uniformly lower than that found in raw Hi-C, yet both methods have their own specific biases and improved normalisation algorithms have the potential to bridge the divergences between the two methods (Beagrie et al., 2017; Chandradoss et al., 2020; Kruse et al., 2020; Liu and Wang, 2019).

Our work underscores previous findings that complex, simultaneous interactions between many partners are a pervasive and under-studied feature of mammalian genome architecture (Beagrie et al., 2017; Quinodoz et al., 2018), although their overall prevalence is still a subject of debate (Olivares-Chauvet et al., 2016). Enhancer-binding transcription factors and RNA Polymerase II have both been reported to form nuclear clusters that could serve as nucleating agents for such multi-partner interactions (Iborra et al., 1996; Liu et al., 2014). More recently, there has been a surge of interest in phase-separated nuclear bodies, which are suggested to facilitate high local concentrations of chromatin-interacting proteins and/or transcriptional regulators (Yoshizawa et al., 2020). The clear expectation is that these condensates should bring together multiple interacting DNA partners, in much the same way as rDNA repeats are brought together in the nucleolus (Pederson, 2011). Heterochromatin has also been reported to form phase-separated condensates (Larson et al., 2017) yet we find these regions to have lower complexity, potentially highlighting a shorter-range role for these interactions.

In conclusion, our development of multiplex-GAM, an improved protocol for rapid, cost-effective generation of GAM datasets enabled us to obtain a deeper GAM dataset for mES cells and to explore the similarities and differences between GAM and Hi-C in greater detail. Reassuringly, the two methods paint broadly similar pictures of nuclear architecture, in particular the distribution of TADs, the segregation of nuclear chromatin into A and B compartments and the importance of CTCF for shaping chromatin interactions. There are differences however, with GAM detecting more and stronger contacts between active chromatin regions and Hi-C emphasising contacts within silent chromatin. These results highlight the utility of GAM for studying contacts of potential gene-regulatory functions, particularly in human disease where such contacts may only be formed in rare cell populations inaccessible to population Hi-C.

Methods

Updated GAM protocol

mES cells were grown and cryoblocks prepared as previously described (Beagrie et al., 2017). 220 nm (green) cryosections were cut with glass knives using a Leica FC7 ultracut cryotome, collected in sucrose droplets (2.1 M in PBS) and transferred to steel frame PEN membrane slides (Leica) UV treated for 45 min prior to use. Slides were washed in sterile-filtered (0.2 µm syringe filter) 1x PBS (3 times, 5 min each), then with sterile-filtered water (3 times, 5 min each). Cresyl violet staining was performed with sterile-filtered cresyl violet (1 % w/v in water, Sigma-Aldrich, C5042) for 10 min, followed by 2 washes with water (30 s each) and air dryed for 15 minutes. Nuclear profiles were laser microdissected into adhesive 8-strip LCM collection caps (Zeiss), with four profiles dissected into each cap. Caps were stored at -20 °C until ready to proceed with whole genome amplification.

Whole genome amplification of DNA from microdissected NPs was performed using the Sigma WGA4 kit using a liquid handling robot (Microlab STARlet, Hamilton). 14.5 µl of lysis and fragmentation mastermix (13 µl H_2O, 1.4 µl lysis and fragmentation buffer, 0.09 µl proteinase K) was added to each well of a 96 well plate, caps with microdissected material were used to close the wells, then the plate was inverted and centrifuged upside-down at 3000 xg for 2 min such that the fragmentation mastermix was collected in the cap. Plates were incubated upside-down for 4 h at 50 °C then inverted and centrifuged right-way-up at 3000 xg for 2 min to collect the extracted DNA in the bottom of the well. Samples were then heat inactivated at 99 °C for 4 min then cooled on ice for 2 min. 4.95 µl library preparation mastermix (3.3 µl library preparation buffer, 1.65 µl library stabilisation solution) was added to each sample, incubated at 95 °C for 2 min, cooled on ice for 2 min then centrifuged at 3000 xg for 2 min. 4.5 µl library preparation enzyme (diluted 3x with H_2O) was added to each tube, then samples were incubated at 16 °C for 20 min, then 24 °C for 20 min, 37 °C for 20 min and 75 °C for 5 min. Finally, 85 µl amplification master mix (11 µl amplification buffer, 66.5 µl H_2O, 7.5 µl WGA polymerase) was added to each tube and samples were amplified by PCR (initial denaturation 95 °C for 3 min, then 24 cycles of denaturation 95 °C for 30 s and annealing/extension 65 °C for 5 min).

Amplified DNA was purified using Ampure XP beads. 61.5 µl beads were mixed with 77 µl amplified sample in a fresh 96-well plate and incubated at room temperature for 5 min. The plate was placed on a magnetic stand for 5 min, then the supernatant was discarded and the beads were washed twice with 200 µl freshly prepared 80% ethanol. After the second ethanol wash was discarded, the beads were air dried for 5 min and then resuspended in 45 µl H_2O and incubated at room temperature for 5 min. The plate was then placed on a magnetic stand and the supernatant transferred to a fresh 96-well plate ready for NGS library prep.

Libraries were prepared using the Illumina Nextera library preparation kit following the manufacturer's instructions. DNA concentration of the final libraries was determined using a Picogreen fluorescence assay (ThermoFisher) and libraries were pooled at equimolar concentration ready for sequencing on an Illumina NextSeq machine.

Data processing

Multiplex-GAM sequencing reads were aligned to the mouse mm9 genome assembly using bowtie2, then positive windows were called by GAMtools v0.0.1 using a fixed read threshold of 4. Normalized linkage disequilibrium (D') matrices at 40 kb genomic resolution were generated by GAMtools (Beagrie and Schueler, 2017).

SLICE analysis

To convert pair or triplet co-segregation frequencies to interaction probabilities (Pi), we computed the segregation probabilities *vi* for a single locus under assumption of spherical shape, with average nuclear radius R (estimated by use of cryosection images as equal to 4.5µm; Beagrie et al., 2017). The co-segregation probabilities *ui* for pairs of loci in a not-interacting state have been estimated from GAM segregation data; for interacting loci, instead, we estimated co-segregation *ti* probabilities by assuming their physical distance less than slice thickness ($h \simeq 220$ nm). From linear combinations of these probabilities, by use of "mean-field" approximation, we computed the probability of locus segregation in a nuclear profile for pairs (*Ni,j*) and triplets (*Ni,j,k*).

The expected number of nuclear profiles *Mi* with 0, 1 or 2 loci, are therefore computed from *Ni,j* probabilities. From these, in turn, it is also possible estimate the co-segregation ratio *M1/(M1 +M2)*, i.e., the fraction of tubes with two loci on all non-empty tubes. Since the equations describing the tubes content depend on the interaction probability *Pi*, the latter can be estimated by fitting the experimental value of co-segregation ratio. The same procedure has been used to estimate the probability of triplet interaction.

To apply SLICE to merged multiplex-GAM dataset, we used a mean field approximation. It consists of introducing a non-integer number of nuclear profiles per tube, obtained as the average of different number of nuclear profiles NPs in the different datasets, weighted with corresponding number of tubes.

Creation of *in silico* merged multiplex-GAM data

Segregation tables (in which each row corresponds to a genomic window, each column to a GAM library and the entries indicate the presence or absence of each window in each NP) were generated from 1NP GAM libraries. A new segregation table was then generated by randomly selecting two, three or four columns from the original table (i.e. 2/3/4x 1NP libraries), combining them into a single column such that the new column is positive if any of the original columns were positive, and removing the columns from the original table. This procedure was performed iteratively until all columns from the original table had been combined. The new, *in silico* combined table was then used for the calculation of normalized linkage disequilibrium matrices.

SLICE enrichment tests

Enrichment of Active/Enhancer/Inactive/Intergenic windows in pairwise SLICE interactions was carried out as previously described (Beagrie et al., 2017). Enrichment analysis of triplet SLICE interactions was carried out as previously described except that 1Mb windows were used instead of TADs.

TAD calling

For calling TADs, we aimed to exclude potential effects of using different TAD callers for GAM and Hi-C. Thus, we applied the insulation square method (Crane et al., 2015) to GAM matrices of normalized linkage disequilibrium scores and to Hi-C matrices of normalized ligation frequencies (GSE35156, Dixon et al., 2012), both at 40 kb resolution. We adjusted the insulation square method to also consider negative values from GAM normalized linkage disequilibrium and applied it to contact matrices of each chromosome (im mean, ids 50000, nt 0.1, yb 1.5, bmoe 3). While TAD sizes were nearly insensitive to the size of the insulation square for Hi-C data (reaching plateau around 500 kb square size; Supplementary Figure 5a), increased sizes of the insulation square produced larger TADs for GAM data. Here, we selected a window size of 400 kb for GAM and Hi-C data which maximizes the agreement between both TAD sets as well as to the HMM TAD boundaries published for the Hi-C dataset (Dixon et al., 2012). To consider differences in the number of detected TAD boundaries, we assessed the agreement between two TAD sets by calculating the product of the distances to the respective closest boundary between both sets with either reference.

We used bedtools v2.27.1 (Quinlan AR and Hall IM, 2010) to check if obtained TAD boundaries were touching or overlapping and merged border ranges keeping their maximum boundary score. In comparisons between TAD boundaries from different datasets we considered boundaries to be matching when the distance reported by bedtools closest was at maximum 1 bin.

We checked for abundance of features at the TAD boundaries centred at their boundary midpoints. For a given genomic mark, we analyzed the mean signal within 500 kb around the identified boundary midpoint in windows of 10 kb resolution using bedtools. We estimated the background by randomizing the boundary positions using chromosome-wise circular shifts.

Generating peak and feature data

We mapped genomic and epigenomic read data to the NCBI Build 37/mm9 reference genome using Bowtie2 v2.1.0 (Langmead et al., 2009). We excluded replicated reads (i.e., identical reads, mapped to the same genomic location) found more often than the 95th percentile of the frequency distribution of each dataset. We obtained peaks using BCP v1.1 (Chen et al, 2012) in transcription factor mode or histone modification mode with default settings. A full list of all features analyzed in this study is given in Supplementary Table 2. We computed mean counts of marks for all genomic 40 kb bins by the bedtools window and intersect functions.

PCA compartments

We computed compartments on GAM and Hi-C data as described (Beagrie et al., 2017; Lieberman-Aiden et al., 2009) or used published compartments definitions (Dixon et al., 2012).

Identification of differential contacts

GAM and Hi-C implement two different approaches to assess chromatin structure and measure underlying contact frequencies. Comparing the value distributions from GAM D' and log-scaled Hi-C ligation frequencies highlights differences in the distributions that need to be considered. To directly compare contact intensities between both methods genome-wide in an unbiased fashion, we devised a strategy where we first normalize contact frequency matrices, subtract normalized contact intensities, and, ultimately, define strong contacts seen in both or at significantly different levels by either of the two methods.

In order to avoid amplification of spurious contacts from noise and zero inflation, we limited our analysis to 4Mb genomic distance. From GAM contact data at 40 kb resolution, we removed all contacts with negative D' values. We also excluded all contacts established between potentially oversampled or undersampled genomic windows. Here, we used the relative number of slices with a positive window (window detection frequency, *wdf*) as a proxy for detectability and removed windows with a *wdf* of less than 5% or above 20%. From the Hi-C data, we excluded all contacts for which zero ligations events were detected. All contacts excluded from any of both datasets were not considered in the definition of differential contacts.

For each chromosome, we applied the z-score transformation to GAM and Hi-C contacts of given distance d. We found this transformation to yield a stable transformation for value intensities from GAM and Hi-C contact matrices (Supplementary Fig. 6c), each resulting in a distribution with a very good fit to a Normal distribution that accounts for the observed decay of mean contact frequency over distance.

To identify the differential contacts between GAM and Hi-C, we computed a delta matrix for each chromosome by subtracting the normalized Hi-C matrix from the normalized GAM matrix. Next, we selected the most differential contacts based on the expected value intensities by fitting a Normal distribution to the distribution of delta values of each chromosome (fitdistrplus package). We defined Hi-C-specific and GAM-specific contacts to be located within the expected 5% and 95% tails of the fitted distributions, which resulted in sets of 231,165 and 265,157 contacts, respectively. Similarly, we defined a set of strong-and-common contacts which have little difference in the normalized value intensities from GAM and Hi-C (delta within 1 sigma) and for which the maximum normalized value intensity from GAM or Hi-C is in the strongest top 10% of each chromosome (total 506,621 contacts).

Feature enrichments within differential contacts

We queried whether contacts identified to be specific for GAM and Hi-C are associated with specific biological features. First, we checked for the occurrence of homotypic and heterotypic feature combinations in the subsets of Hi-C-specific, GAM-specific, strong-and-common contacts. We annotated 50.29%, 69.58%, and 60.28% of contacts with feature pairs, respectively. We established feature co-occurrence relative to genomic background which was randomly selected using 5% of all non-zero contacts observed by GAM and Hi-C from each chromosome.

To assess the amplification of genomic feature pairs in GAM-specific, Hi-C-specific, and strong-and-common contacts, we produced three permutations of random background sets for each of the foreground sets. Here, we randomly sampled the same number of contacts out of all contacts of the same chromosome with the same genomic distance. To determine whether feature combinations are observed in the foreground sets more frequently than to be expected, we computed the amplification (relative frequency) in contrast to the matched background.

Pairs of different features can often be found co-present at the same anchor points of a contact. We applied the UpSetR package (Conway et al., 2017) to the sets of contacts from GAM-specific, Hi-C-specific, strong-and-common, and the genome-wide background and plotted the abundance of a feature pair according to the percentile of feature occurrence along with the number of observed colocalization events between pairs of features.

To directly compare GAM-specific and Hi-C-specific contacts and to see whether both sets can be distinguished using the associated feature pairs, we trained a Random Forest model (sklearn 0.19.2, 100 trees, no pruning) and extracted the top 12 feature pairs that were most informative for binary classification based on the Gini importance criterion.

Analysis of GAM-preferred and Hi-C preferred regions

We assessed for each genomic 40 kb window the preference towards preferentially producing GAM-specific contacts or Hi-C specific contacts. First, we counted how often a window was an anchor point for contacts of the GAM-specific or Hi-C-specific subsets. Next, we calculated the absolute difference between both counts and estimated a 90% percentile cutoff for each chromosome. We considered genomic windows above this threshold to either hold mostly GAM-specific contacts or mostly Hi-C-specific contacts. In total, this resulted in 6,520 windows to be labelled as GAM-preferred regions by having predominantly GAM-specific contacts, and 5,926 Hi-C-preferred regions with a much higher count of Hi-C-specific contacts over GAM-specific contacts. Similarly, we identified genomic regions that are equally well detected by GAM and Hi-C. Here, we counted for each genomic window the number of anchor points from contacts of the strong-and-common set and selected the top 10% genomic windows with highest counts from each chromosome.

Next, we assessed gene density and transcriptional activity in groups of genomic regions using published gene annotations and mESC-46C TPM values (Ferrai et al., 2017). We transferred provided mm10 gene positions to mm9 using UCSC liftover (Kuhn et al., 2013) and assigned genes to genomic windows of 40 kb using bedtools intersect. We annotated lamina associations within 40 kb genomic regions according to mESC LaminB1 HMM calls (Peric-Hupkes et al., 2010). The genome-wide LAD ratio was computed by the number of positive HMM state calls over the total number of bins. For markers of TFs, histone modifications, and RNA Polymerase II states, we used 40 kb window classification for peak and feature presence (Supplementary Table 2) and counted the number of positive windows in each subset.

Analysis of interaction complexity

We used SLICE to compute the three-way probability of interaction (Pi_{ABC}) for all potential 1Mb intrachromosomal triplets from the GAM-1250 dataset. We define complexity as the mean Pi_{ABC} – either the mean over all combinations of “B” and “C” bins for a given “A” bin (where complexity is being calculated for a genomic region, Fig. 7c,d) or the mean over all

"C" bins for a given "A" and "B" bin (where complexity is calculated for a pairwise contact, Fig. 7e).

For each genomic window labelled as Hi-C preferred regions, common regions, or GAM-preferred regions, we checked for the compartment assignment and correlated the outcome with the complexity at the 1Mb genomic window. Similarly, we estimated the complexity of genomic and epigenetic features by subsetting 40 kb genomic windows according to the presence of TFs, histone modifications, and RNA polymerase II states and presenting the complexity of the respective 1Mb genomic window.

Acknowledgments

The authors thank all lab members and the 4D nucleome consortium for helpful discussions. We thank Warren Winick-Ng for providing illustrations in Fig. 1c,d. We also deeply appreciate the feedback from Teresa Szczepińska on the processing of differential contacts. AP acknowledges support from the Helmholtz Association (Germany). AP and MN acknowledge support from the National Institutes of Health Common Fund 4D Nucleome Program grant U54DK107977, and the Berlin Institute of Health (BIH). AP acknowledges support from the Deutsche Forschungsgemeinschaft (DFG; German Research Foundation) under Germany's Excellence Strategy - EXC-2049 - 390688087. MN thanks for support from CINECA ISCRA Grant HP10CYFPS5 and HP10CRTY8P, by computer resources at INFN and Scope at the University of Naples (MN). LW acknowledges the support of Ohio University's GERB program. RAB is supported by the Wellcome Trust (209181/Z/17/Z).

Author contributions

AP and MN devised the multiplex-GAM strategy;
RAB produced GAM datasets;
RAB, AK and RK optimised the experimental protocol;
RAB performed GAM data processing, QC and *in-silico* merging experiments;
DCAK performed cryoFISH experiments;
CA, AS, SB, AMC, and MN developed and implemented the updated SLICE model;
CA and AS applied SLICE to find optimal experimental parameters and performed SLICE analysis of GAM data;
RAB performed enrichment analyses for SLICE contact pairs and triplets;
CJT and MS performed TAD boundary analysis;
CJT and AK processed epigenetic and genomic data;
CJT and MS devised pipeline to extract differential contacts; CJT generated randomized contact sets;
YZ and YL developed and applied the pipeline for feature pair presence and enrichments over background;
CB performed Random Forest discrimination tests;
CB and CJT performed feature pair co-localization tests;
CJT identified and analysed preferred regions;
RAB and CJT assessed complexity of contacts, preferred regions, and feature-positive genomic windows;
AP supervised GAM and FISH experiments and bioinformatics analyses;
LW supervised feature enrichment analyses in specific contacts;
MN supervised SLICE development;
AP, RAB, CJT, AK, CA, AS, YZ, CB, LW, and MN contributed to the interpretation of the results;
RAB wrote the first draft of the manuscript;

RAB and CJT designed the figures;
RAB, CJT, and AP wrote the manuscript;
All authors provided critical feedback and helped revise the manuscript.

The authors consider RAB, CJT and CA to have contributed equally to this work.

Competing interests

A.P., M.N., R.A.B., A.S. hold a patent on 'Genome Architecture Mapping': Pombo, A., Edwards, P. A. W., Nicodemi, M., Beagrie, R. A. & Scialdone, A. Patent PCT/EP2015/079413 (2015).

Materials & Correspondence

Correspondence and material requests should be addressed to ana.pombo@mdc-berlin.de; mario.nicodemi@na.infn.it ; welch@ohio.edu

Supplementary Table 2

Repetitive DNA elements			
	LINEs, SINEs, LTR, simple repeats, tRNAs	RepeatMasker/UCSC Table Browser	
Constitutive heterochromatin			
	H3K9me3	Bilodeau et al., 2009	GSE18371
	H3K20me3	Mikkelsen et al., 2007	GSE12241
CTCF			
	CTCF	Shen et al., 2012	GSE29184
TFs			
	Nanog	Marson et al., 2008	GSE11724
	Oct4	Marson et al., 2008	GSE11724
	Sox2	Marson et al., 2008	GSE11724
	Tcf3	Marson et al., 2008	GSE11724
	ZNF384	ENCODE	
	MAFK	ENCODE	
	ZC3H11A	ENCODE	
Enhancers			
	Enhancers	Cruz-Molina et al., 2017	
	Super enhancers	Whyte et al., 2013	
Enhancer regulators			
	Med12	Kagey et al., 2010	GSE22557
	p300	Shen et al., 2012	GSE29184
	H3K27ac	Shen et al., 2012	GSE29184

RNA polymerase II and transcription-related histone marks

RNAPII-S7p	Ferrai et al., 2017	GSE94364
RNAPII-S5p	Ferrai et al., 2017	GSE94364
H3K4me3	Shen et al., 2012	GSE29184
RNAPII-S2p	Brookes et al., 2012	GSE34520
H3K36me3	Marson et al., 2008	GSE11724
H3K79me2	Marson et al., 2008	GSE11724

Facultative heterochromatin

Ezh2	Peng et al., 2009	GSE18776
H3K27me3	Ferrai et al., 2017	GSE94364

LADs

mESC HMM state calls	Peric-Hupkes et al., 2010	GSE17051

References

Andersson, R., and Sandelin, A. (2020). Determinants of enhancer and promoter activities of regulatory elements. Nat. Rev. Genet. *21*, 71–87.

Beagan, J.A., and Phillips-Cremins, J.E. (2020). On the existence and functionality of topologically associating domains. Nat. Genet. *52*, 8–16.

Beagrie, R.A., and Schueler, M. (2017). GAMtools: an automated pipeline for analysis of Genome Architecture Mapping data Addresses : Keywords.

Beagrie, R.A., Scialdone, A., Schueler, M., Kraemer, D.C.A., Chotalia, M., Xie, S.Q., Barbieri, M., de Santiago, I., Lavitas, L., Branco, M.R., et al. (2017). Complex multi-enhancer contacts captured by genome architecture mapping. Nature *543*, 519–524.

Bonev, B., Cohen, N.M., Szabo, Q., Hugnot, J., Tanay, A., Cavalli, G., Bonev, B., Cohen, N.M., Szabo, Q., Fritsch, L., et al. (2017). Multiscale 3D Genome Rewiring during Mouse Article Multiscale 3D Genome Rewiring during Mouse Neural Development. Cell *171*, 557.e1-557.e24.

Chandradoss, K.R., Guthikonda, P.K., Kethavath, S., Dass, M., Singh, H., Nayak, R., Kurukuti, S., and Sandhu, K.S. (2020). Biased visibility in Hi-C datasets marks dynamically regulated condensed and decondensed chromatin states genome-wide. BMC Genomics *21*, 175.

Conway, J.R., Lex, A., and Gehlenborg, N. (2017). UpSetR: an R package for the visualization of intersecting sets and their properties. Bioinformatics *33*, 2938–2940.

Crane, E., Bian, Q., McCord, R.P., Lajoie, B.R., Wheeler, B.S., Ralston, E.J., Uzawa, S., Dekker, J., and Meyer, B.J. (2015). Condensin-driven remodelling of X chromosome topology during dosage compensation. Nature *523*, 240–244.

Dixon, J.R., Selvaraj, S., Yue, F., Kim, A., Li, Y., Shen, Y., Hu, M., Liu, J.S., and Ren, B. (2012). Topological domains in mammalian genomes identified by analysis of chromatin

interactions. Nature *485*, 376–380.
Downes, D.J., Gosden, M.E., Telenius, J., Carpenter, S.J., Nussbaum, L., Ornellas, S. De, Sergeant, M., Eijsbouts, C.Q., Schwessinger, R., Kerry, J., et al. (2020). Targeted high-resolution chromosome conformation capture at genome-wide scale. BioRxiv 2020.03.02.953745.
Ferrai, C., Torlai Triglia, E., Risner-Janiczek, J.R., Rito, T., Rackham, O.J., Santiago, I., Kukalev, A., Nicodemi, M., Akalin, A., Li, M., et al. (2017). RNA polymerase II primes Polycomb-repressed developmental genes throughout terminal neuronal differentiation. Mol. Syst. Biol. *13*, 946.
Fraser, J., Ferrai, C., Chiariello, A.M., Schueler, M., Rito, T., Laudanno, G., Barbieri, M., Moore, B.L., Kraemer, D.C., Aitken, S., et al. (2015). Hierarchical folding and reorganization of chromosomes are linked to transcriptional changes in cellular differentiation. Mol. Syst. Biol. *11*, 852–852.
Gavrilov, A., Razin, S. V, and Cavalli, G. (2015). In vivo formaldehyde cross-linking: it is time for black box analysis. Brief. Funct. Genomics *14*, 163–165.
Gavrilov, A. a, Gushchanskaya, E.S., Strelkova, O., Zhironkina, O., Kireev, I.I., Iarovaia, O. V, and Razin, S. V (2013). Disclosure of a structural milieu for the proximity ligation reveals the elusive nature of an active chromatin hub. Nucleic Acids Res. *41*, 3563–3575.
Guillot, P. V, Xie, S.Q., Hollinshead, M., and Pombo, A. (2004). Fixation-induced redistribution of hyperphosphorylated RNA polymerase II in the nucleus of human cells. Exp. Cell Res. *295*, 460–468.
Iborra, F.J., Pombo, A., Jackson, D. a, and Cook, P.R. (1996). Active RNA polymerases are localized within discrete transcription “factories’’ in human nuclei.” J. Cell Sci. *109*, 1427–1436.
Kempfer, R., and Pombo, A. (2020). Methods for mapping 3D chromosome architecture. Nat. Rev. Genet. *21*, 207–226.
Kruse, K., Hug, C.B., and Vaquerizas, J.M. (2020). FAN-C : a feature-rich framework for the analysis and visualisation of C data. BioRxiv 1–10.
Kuhn, R.M., Haussler, D., and Kent, W.J. (2013). The UCSC genome browser and associated tools. Brief. Bioinform. *14*, 144–161.
Larson, A.G., Elnatan, D., Keenen, M.M., Trnka, M.J., Johnston, J.B., Burlingame, A.L., Agard, D.A., Redding, S., and Narlikar, G.J. (2017). Liquid droplet formation by HP1α suggests a role for phase separation in heterochromatin. Nature *547*, 236–240.
Lieberman-Aiden, E., van Berkum, N.L., Williams, L., Imakaev, M., Ragoczy, T., Telling, A., Amit, I., Lajoie, B.R., Sabo, P.J., Dorschner, M.O., et al. (2009). Comprehensive mapping of long-range interactions reveals folding principles of the human genome. Science *326*, 289–293.
Liu, T., and Wang, Z. (2019). normGAM: an R package to remove systematic biases in genome architecture mapping data. BMC Genomics *20*, 1006.
Liu, Z., Legant, W.R., Chen, B.-C., Li, L., Grimm, J.B., Lavis, L.D., Betzig, E., and Tjian, R. (2014). 3D imaging of Sox2 enhancer clusters in embryonic stem cells. Elife *3*, 1–29.
Nora, E.P., Lajoie, B.R., Schulz, E.G., Giorgetti, L., Okamoto, I., Servant, N., Piolot, T., van Berkum, N.L., Meisig, J., Sedat, J., et al. (2012). Spatial partitioning of the regulatory landscape of the X-inactivation centre. Nature *485*, 381–385.
O'Sullivan, J.M., Hendy, M.D., Pichugina, T., Wake, G.C.G., and Langowski, J. (2013). The statistical-mechanics of chromosome conformation capture. Nucleus *4*, 390–398.
Olivares-Chauvet, P., Mukamel, Z., Lifshitz, A., Schwartzman, O., Elkayam, N.O., Lubling, Y., Deikus, G., Sebra, R.P., and Tanay, A. (2016). Capturing pairwise and multi-way chromosomal conformations using chromosomal walks. Nature 1–21.
Oudelaar, A.M., Davies, J.O.J., Downes, D.J., Higgs, D.R., and Hughes, J.R. (2017). Robust

detection of chromosomal interactions from small numbers of cells using low-input Capture-C. Nucleic Acids Res. *45*, e184–e184.

Pederson, T. (2011). The nucleolus. Cold Spring Harb. Perspect. Biol. *3*, 1–15.

Peric-Hupkes, D., Meuleman, W., Pagie, L., Bruggeman, S.W.M., Solovei, I., Brugman, W., Gräf, S., Flicek, P., Kerkhoven, R.M., van Lohuizen, M., et al. (2010). Molecular Maps of the Reorganization of Genome-Nuclear Lamina Interactions during Differentiation. Mol. Cell *38*, 603–613.

Quinodoz, S.A., Ollikainen, N., Tabak, B., Palla, A., Schmidt, J.M., Detmar, E., Lai, M.M., Shishkin, A.A., Bhat, P., Takei, Y., et al. (2018). Higher-Order Inter-chromosomal Hubs Shape 3D Genome Organization in the Nucleus. Cell *174*, 744-757.e24.

Sexton, T., Yaffe, E., Kenigsberg, E., Bantignies, F., Leblanc, B., Hoichman, M., Parrinello, H., Tanay, A., and Cavalli, G. (2012). Three-dimensional folding and functional organization principles of the Drosophila genome. Cell *148*, 458–472.

Shaban, H.A., and Seeber, A. (2020). Monitoring the spatio-temporal organization and dynamics of the genome. Nucleic Acids Res. *48*, 3423–3434.

Williamson, I., Berlivet, S., Eskeland, R., Boyle, S., Illingworth, R.S., Paquette, D., and Bickmore, W.A. (2014). Spatial genome organization : contrasting views from chromosome conformation capture and fluorescence in situ hybridization. Genes Dev. *28*, 2778–2791.

Winick-Ng, W., Kukalev, A., Harabulā, I., Zea Redondo, L., Meijer, M., Serebreni, L., Bianco, S., Szabo, D., Chiariello, A.M., Irastorza Azcarate, I., et al. (2020). Cell-type specialization in the brain is encoded by specific long-range chromatin topologies. BioRxiv 2020.04.02.020990.

Yoshizawa, T., Nozawa, R.-S., Jia, T.Z., Saio, T., and Mori, E. (2020). Biological phase separation: cell biology meets biophysics. Biophys. Rev. *12*, 519–539.

Supplementary Figures

Supplementary Figure 1

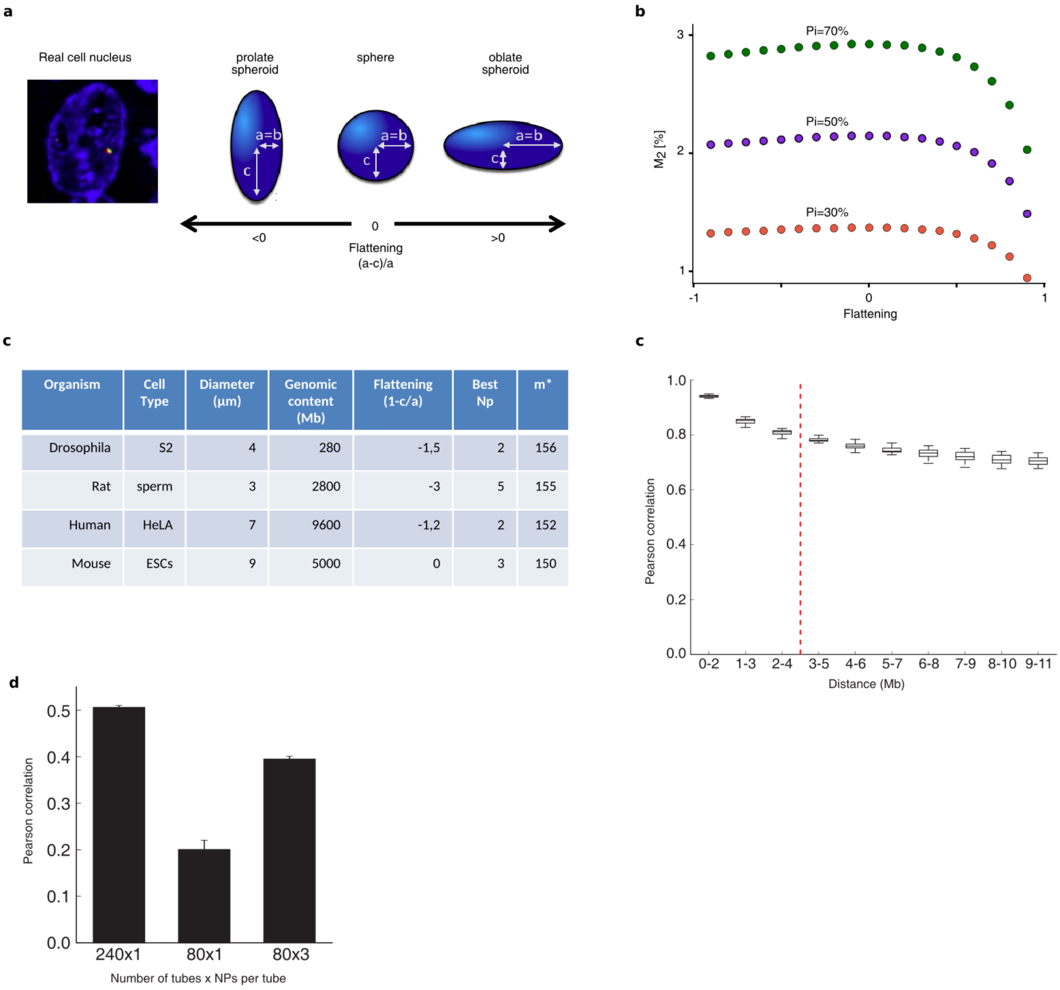

Organism	Cell Type	Diameter (μm)	Genomic content (Mb)	Flattening (1-c/a)	Best Np	m*
Drosophila	S2	4	280	-1,5	2	156
Rat	sperm	3	2800	-3	5	155
Human	HeLA	7	9600	-1,2	2	152
Mouse	ESCs	9	5000	0	3	150

a, SLICE can be generalized to account for complex nuclear shapes. As a case study, we considered spheroids (i.e., ellipsoids with two equal axes), which we parametrized by the flattening parameter (the relative difference of the radii). **b**, Co-segregation frequency of pairs of loci (*M2*) derived by SLICE as function of the flattening parameter in spheroidal nuclei of constant volume, for different values of interaction frequency (*Pi*) given slice thickness (*h*) of 220nm, resolution of 30 kb, detection efficiency of 1 and genomic distances of 50Mb. **c**, Optimal GAM experimental parameters for different cell types given *h*=220nm, Pi=30% detection efficiency of 1 and genomic distance of 50Mb. The nuclear size and shape of the cell types were obtained from published results (Auger et al., 2004; Brandt et al., 2006; Iborra and Buckle, 2008; Landry et al., 2013). **d**, Correlation of GAM datasets containing single nuclear profiles with GAM datasets where the same NPs are merged *in silico* in sets of three, stratified by distance. **e**, Correlation between two GAM datasets of 240 x 1NP libraries (left) compared to the correlation of two datasets of 80 x 1NP libraries (middle) and two replicates of 80 x 3NP (right, same number of NPs as left bar, same sequencing cost as middle bar).

Supplementary Figure 2

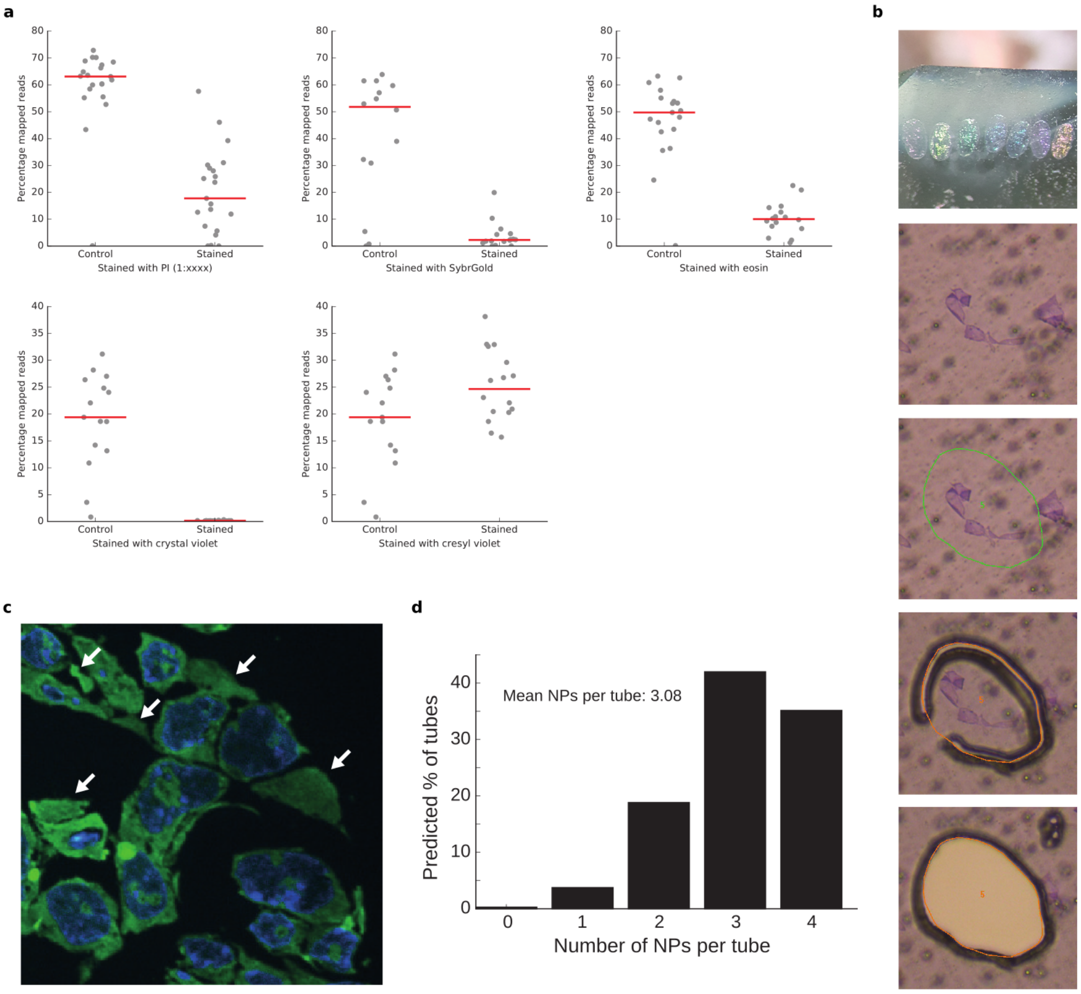

a, Effect of various staining protocols on downstream DNA extraction (top row: propidium iodide, SYBR® Gold, Eosin; bottom row: crystal violet, cresyl violet). **b**, Top panel: cryosection thickness can be identified from the section's colour. Bottom panels: cresyl violet staining improves the identification of NPs during laser microdissection. **c**, Example mES cell cryosection visualized by confocal fluorescence microscopy, DNA stained with DAPI is shown in blue and RNA stained with SYTO® RNASelectTM dye is shown in green. White arrows indicate cellular profiles that do not intersect nuclei. **d**, Binomial distribution showing the expected number of profiles per sample that intersect nuclei across a collection of samples each with four cellular profiles.

Supplementary Figure 3

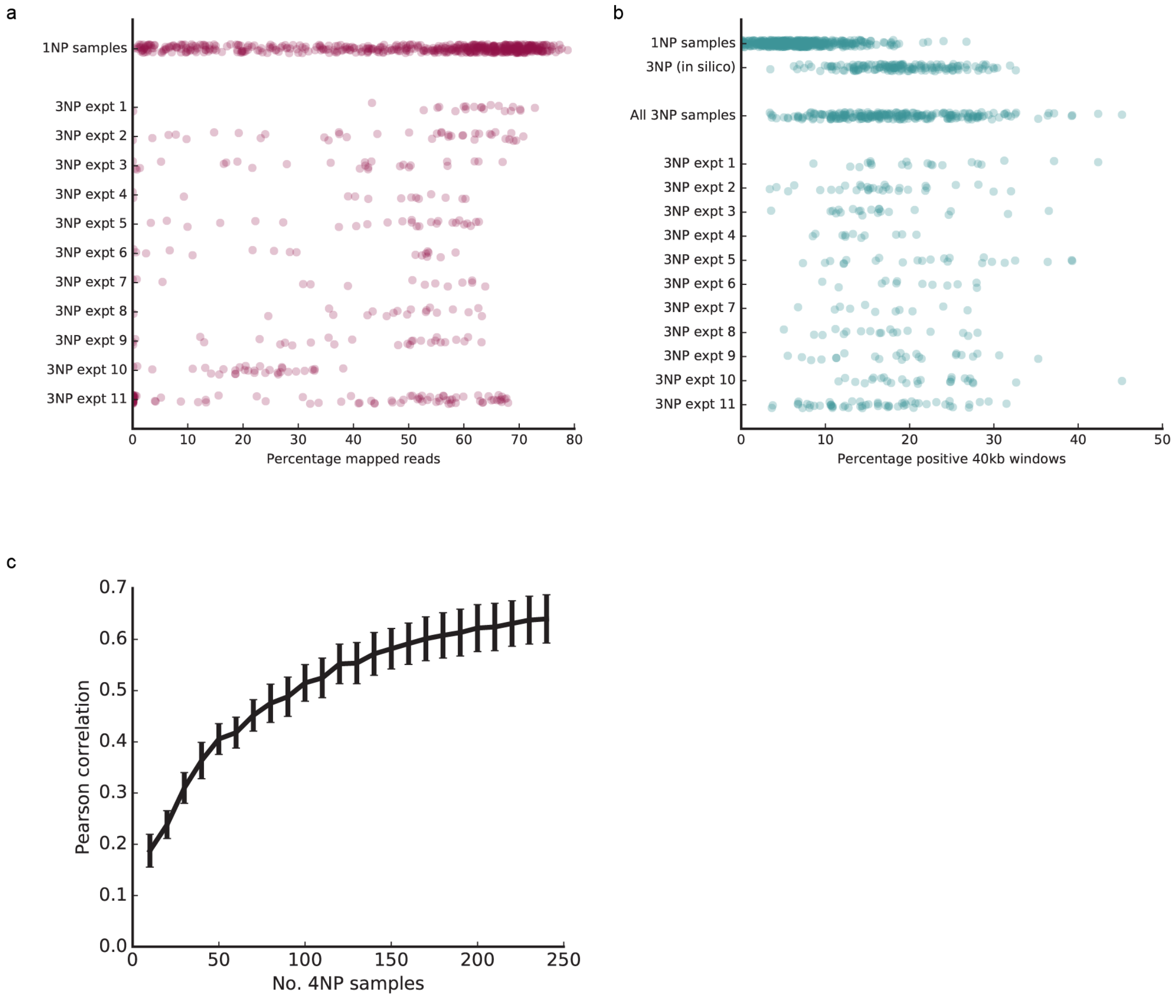

a, Percentage of reads mapping to the mouse genome for 1NP libraries and for 3NP libraries separated by experimental batch. **b**, Percentage of positive 40 kb windows or 1NP libraries, for 1NP libraries combined into 3NP libraries *in silico* and for 3NP libraries (i.e. four cellular profiles dissected into each tube with binomial expectation that, on average, three profiles in each tube intersect the nucleus; see Supplementary Fig. 2d,e) separated by experimental batch. **c**, Pearson correlation between normalized linkage matrices calculated from increasing subsets of 3NP libraries and matrix calculated from 481 x 1NP libraries.

Supplementary Figure 4

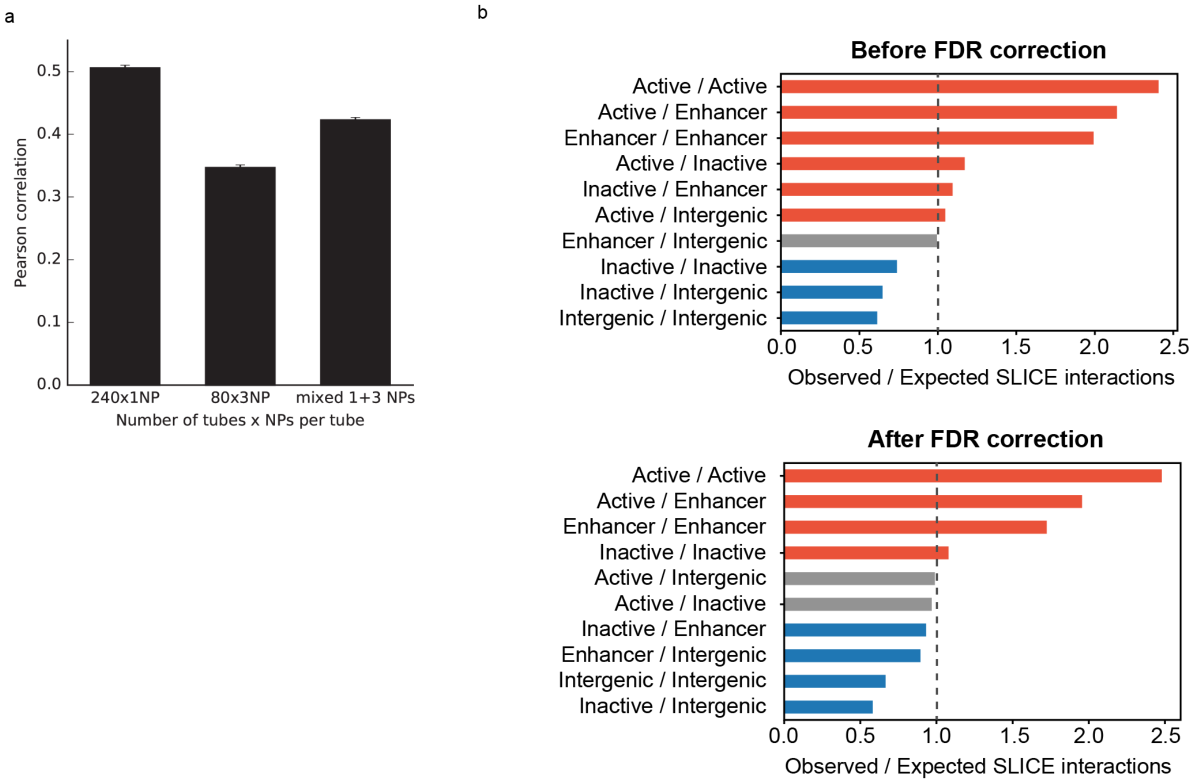

a, Correlation between two GAM datasets of 240 x 1NP libraries (left) compared to the correlation of two replicates of 80 x 3NP (middle) and a mixture of 96 x 1NP and 48 x 3NP (right, same number of total NPs mixed in the same ratio as the GAM-1250 dataset). Left and middle bars are the same as in Supplementary Fig. 1e. **b**, Enrichment analysis of pairwise interactions identified by SLICE involving active, inactive, intergenic or enhancer regions for the merged GAM-1250 dataset either before (left) or after (right) false discovery rate correction.

Supplementary Figure 5

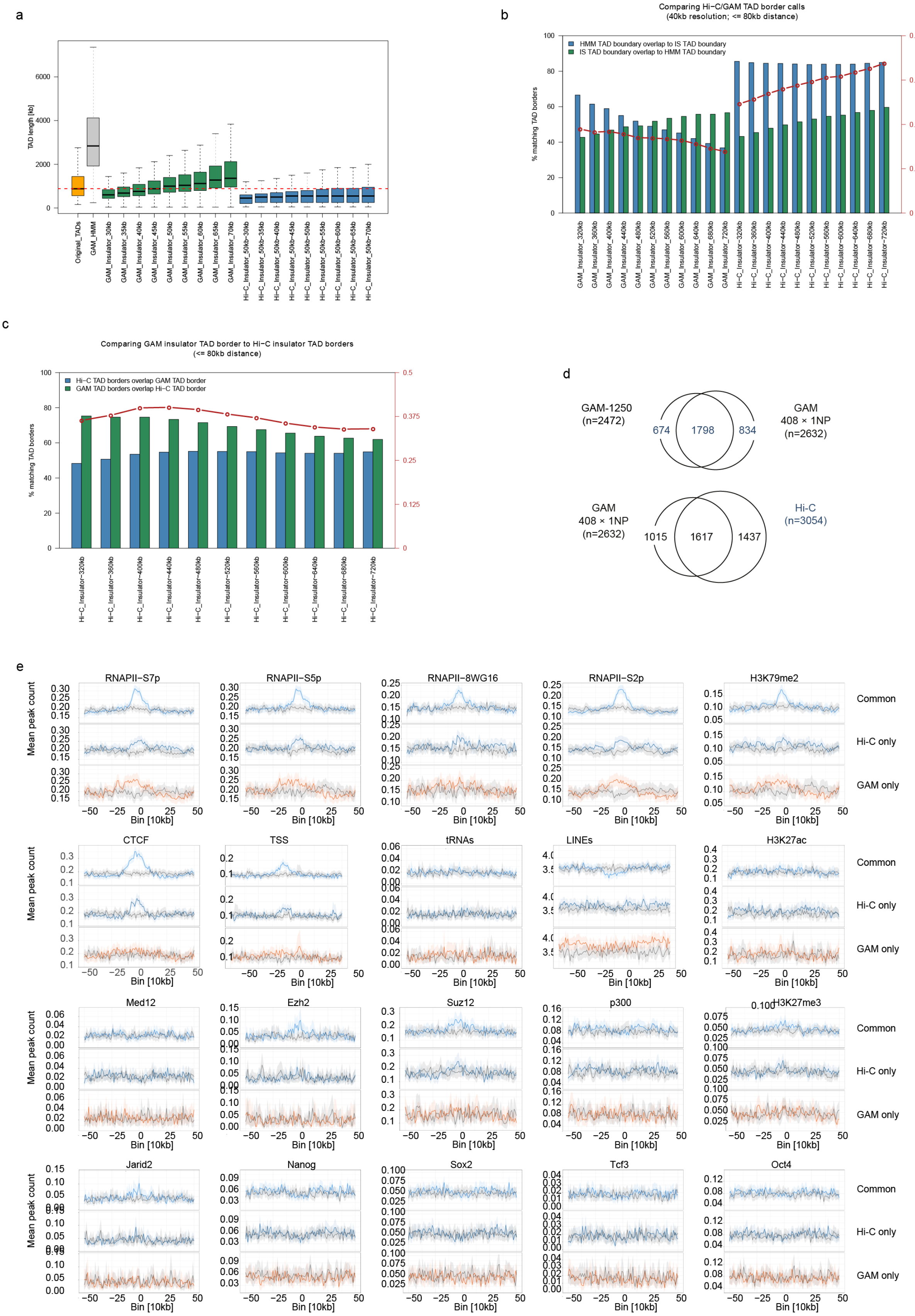

a, TAD length for published Hidden Markov Model (HMM) TAD boundaries from mES cells (grey), TAD boundaries called from GAM-1250 dataset by HMM (first orange bar) or by insulation score

(IS) with increasing insulation square size (remaining orange bars), and TAD boundaries called from Hi-C data using IS with increasing insulation square size (blue bars). **b**, Left: Percentage of published Hi-C HMM TAD boundaries overlapping a GAM IS boundary (blue) and percentage of GAM IS boundaries overlapping a Hi-C HMM boundary (green) for increasing insulation square size. Right: same as left panel but for Hi-C IS boundaries. Optimization score is the product of the two overlap fractions (red line). **c**, Percentage of Hi-C IS TAD boundaries overlapping a GAM IS TAD boundary (blue) or vice versa (green) with increasing insulation square size. **d**, Top: overlap of IS TAD boundaries calculated from GAM-1250 and the published GAM dataset for mES. Bottom: Overlap of IS TAD boundaries calculated from Hi-C data or from published GAM dataset. e, Aggregated counts for transcription factor binding sites and epigenetic marks centred at TAD boundary sites. Common, Hi-C-specific, GAM-specific boundaries are shown in dark blue, blue, and red, respectively, grey values are based on randomized boundary positions of each category.

Supplementary Figure 6

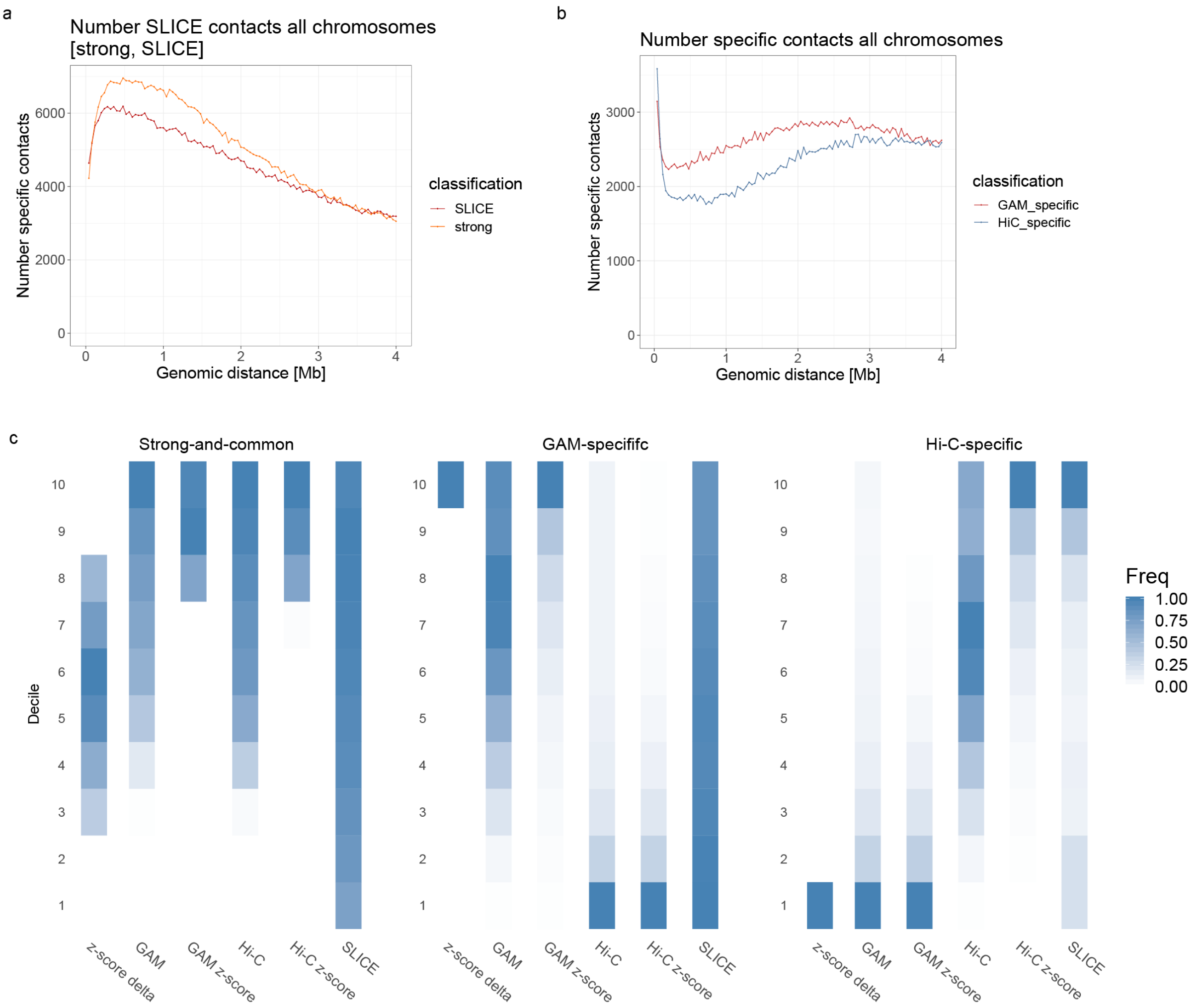

a, Distribution by genomic distance of GAM-specific (red) and Hi-C specific (blue) contacts. **b**, distribution by genomic distance of SLICE interactions (red) and strong-and-common contacts (orange). **c**, Decentile distributions of contact intensities before and after z-score normalization for the sets of GAM-specific contacts, Hi-C-specific contacts, and Strong-and-common contacts.

Supplementary Figure 7

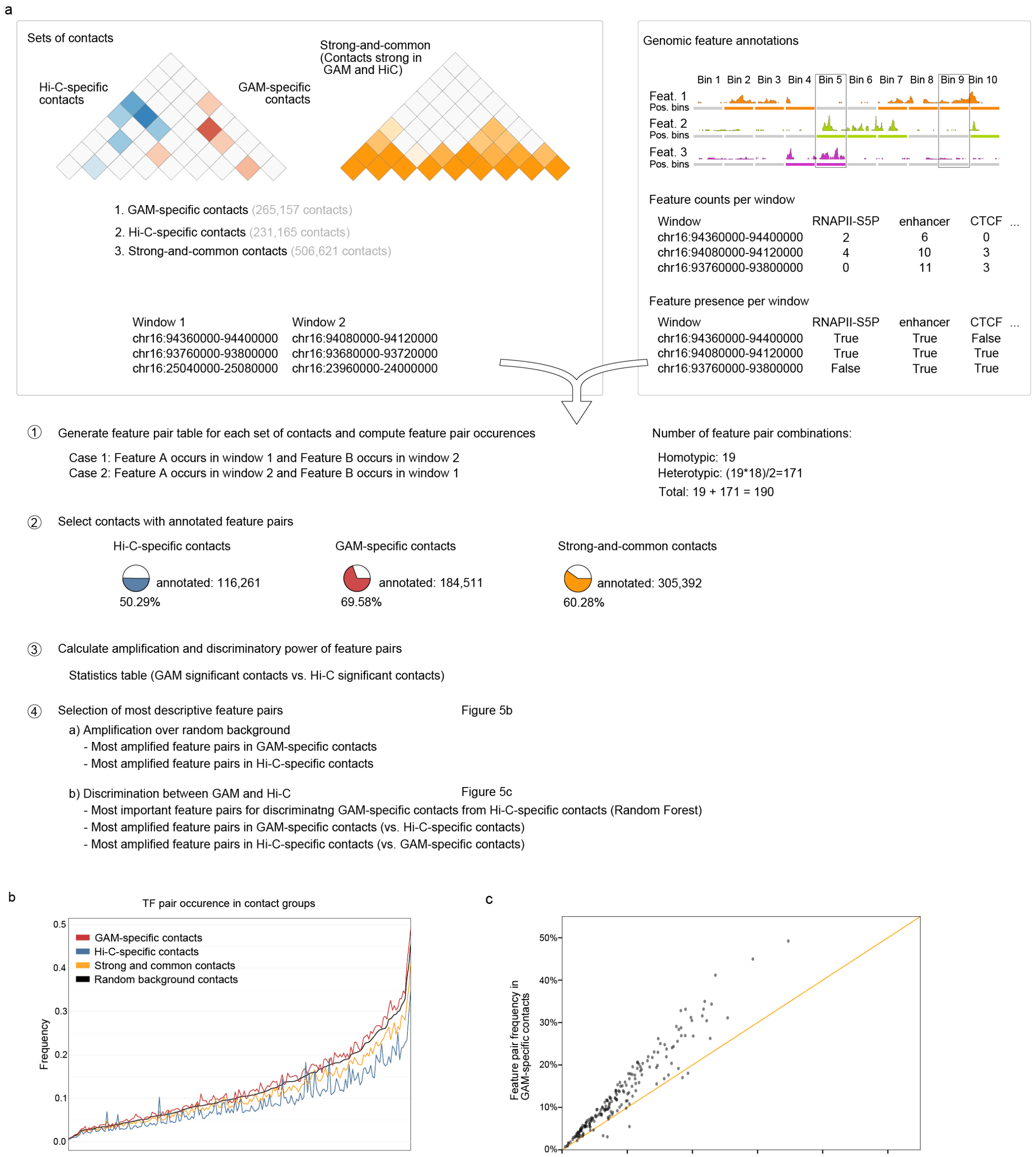

1. GAM-specific contacts (265,157 contacts)
2. Hi-C-specific contacts (231,165 contacts)
3. Strong-and-common contacts (506,621 contacts)

Window 1	Window 2
chr16:94360000-94400000	chr16:94080000-94120000
chr16:93760000-93800000	chr16:93680000-93720000
chr16:25040000-25080000	chr16:23960000-24000000

Feature counts per window

Window	RNAPII-S5P	enhancer	CTCF	...
chr16:94360000-94400000	2	6	0	
chr16:94080000-94120000	4	10	3	
chr16:93760000-93800000	0	11	3	

Feature presence per window

Window	RNAPII-S5P	enhancer	CTCF	...
chr16:94360000-94400000	True	True	False	
chr16:94080000-94120000	True	True	True	
chr16:93760000-93800000	False	True	True	

① Generate feature pair table for each set of contacts and compute feature pair occurences

Case 1: Feature A occurs in window 1 and Feature B occurs in window 2
Case 2: Feature A occurs in window 2 and Feature B occurs in window 1

Number of feature pair combinations:

Homotypic: 19
Heterotypic: (19*18)/2=171
Total: 19 + 171 = 190

② Select contacts with annotated feature pairs

Hi-C-specific contacts	GAM-specific contacts	Strong-and-common contacts
annotated: 116,261	annotated: 184,511	annotated: 305,392
50.29%	69.58%	60.28%

③ Calculate amplification and discriminatory power of feature pairs

Statistics table (GAM significant contacts vs. Hi-C significant contacts)

④ Selection of most descriptive feature pairs — Figure 5b

a) Amplification over random background
- Most amplified feature pairs in GAM-specific contacts
- Most amplified feature pairs in Hi-C-specific contacts

b) Discrimination between GAM and Hi-C — Figure 5c
- Most important feature pairs for discriminatng GAM-specific contacts from Hi-C-specific contacts (Random Forest)
- Most amplified feature pairs in GAM-specific contacts (vs. Hi-C-specific contacts)
- Most amplified feature pairs in Hi-C-specific contacts (vs. GAM-specific contacts)

b
TF pair occurence in contact groups
GAM-specific contacts
Hi-C-specific contacts
Strong and common contacts
Random background contacts
Frequency
0.0
0.1
0.2
0.3
0.4
0.5
Feature pairs (ranked)
c
Feature pair frequency in GAM-specific contacts
0%
10%
20%
30%
40%
50%
0%
10%
20%
30%
40%
50%

a, Strategy for detecting enrichment of feature pairs within sets of specific contacts. **b**, Frequency of feature pair combinations in the sets of GAM-specific contacts, Hi-C-specific contacts, and strong-and-common contacts ordered by the expected presence in the genomic background (5% random sample of contacts). **c**, Correlation of observed frequencies of feature pairs between GAM-specific and Hi-C-specific contacts.

Supplementary Figure 8

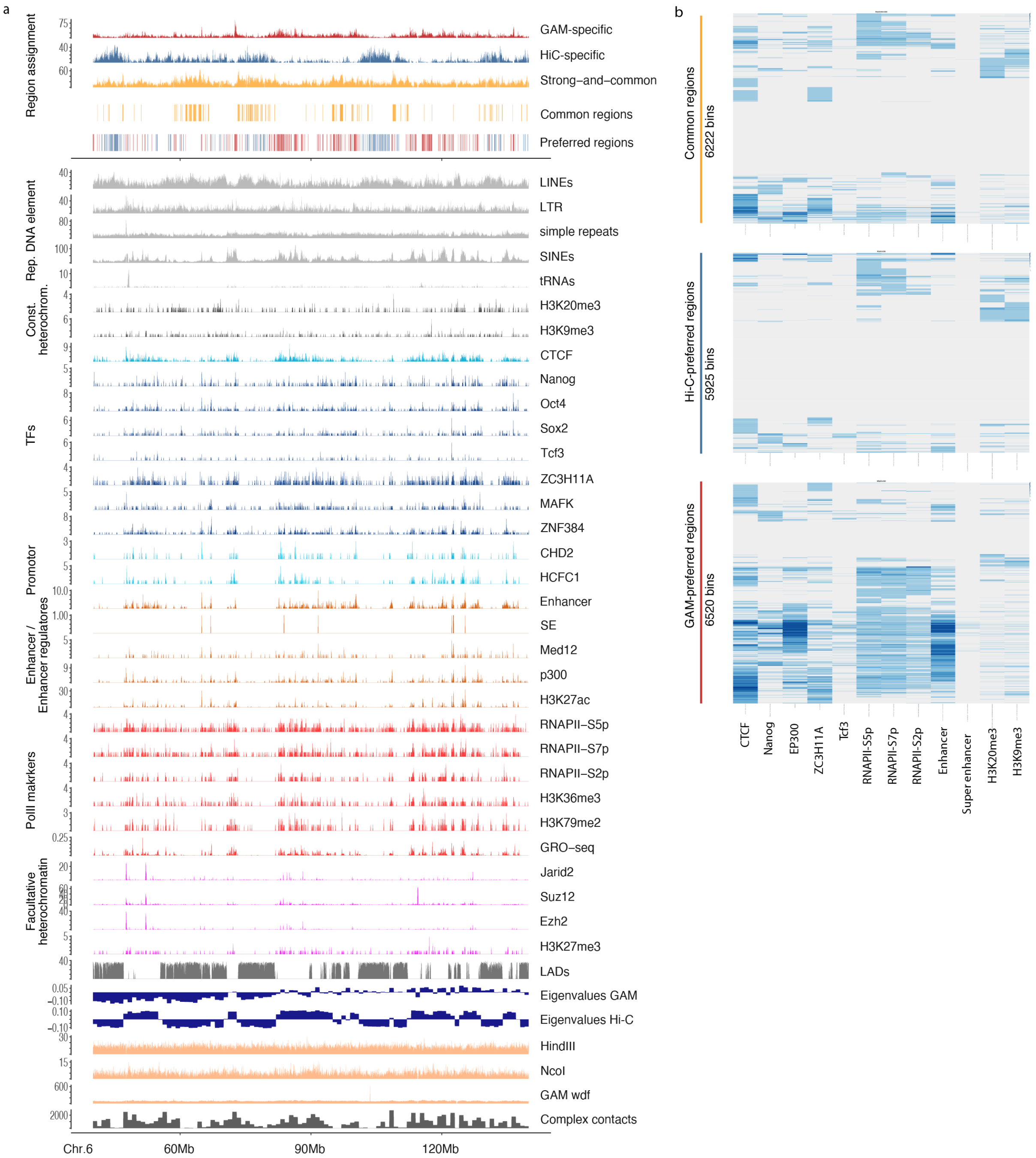

a, Feature tracks and assignment of genomic regions having mostly GAM-specific contacts (GAM-preferred regions) or Hi-C-specific contacts (Hi-C-preferred regions). **b**, Heatmap representation for feature presence at GAM-preferred regions, Hi-C-preferred regions) or regions with contacts found at similar intensity by both methods (common regions).

Supplementary Figure 9

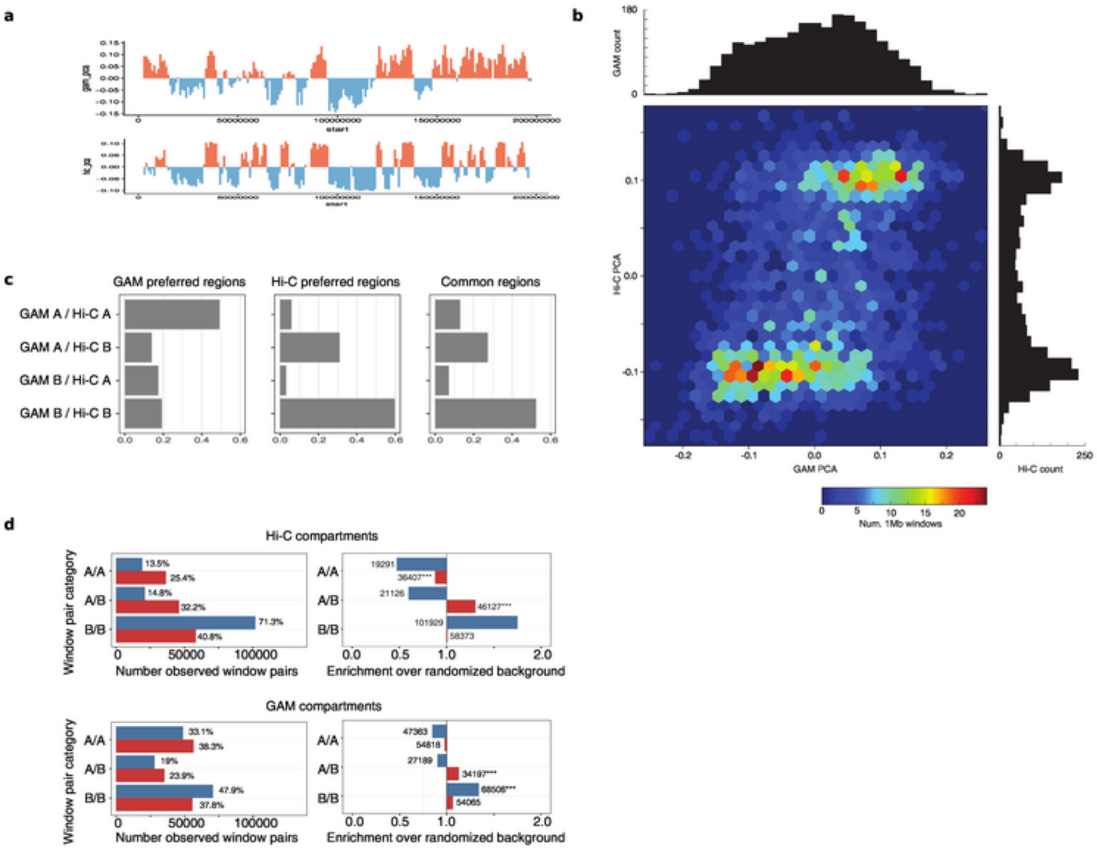

a, PCA eigenvalue values from GAM and Hi-C for mouse chromosome 1. **b**, Correlation heatmap for GAM and Hi-C eigenvalues. A small subset of windows assigned to the A compartment by GAM (positive eigenvalues) are assigned to the B compartment by Hi-C (negative eigenvalues). Value histograms indicate that Hi-C eigenvalues are clearly bimodal distributed while GAM finds an increased number of eigenvalues in the transition zone. **c**, Agreement between GAM and Hi-C compartment calls for GAM-preferred (left), Hi-C preferred (middle) and common (right) regions. **d**, Absolute number (left) and enrichment over random background (right) of compartment combinations observed in the sets of Hi-specific contacts (blue) and GAM-specific contacts (red). Compartment definitions of 1Mb resolution were obtained from Hi-C data (top) or GAM data (bottom).